applied sciences

MDPI

Article

Hygro-Thermo-Mechanical Analysis of Brick Masonry Walls Subjected to Environmental Actions

Rafael Ramirez [1], Bahman Ghiassi [2], Paloma Pineda [3] and Paulo B. Lourenço [1,*]

[1] Department of Civil Engineering, ISISE, ARISE, University of Minho, Campus de Azurem s/n, 4800-085 Guimaraes, Portugal
[2] Department of Civil Engineering, School of Engineering, University of Birmingham, Birmingham B15 2TT, UK
[3] Department of Building Structures and Geotechnical Engineering, University of Seville, Avenida Reina Mercedes 2, 41012 Seville, Spain
* Correspondence: pbl@civil.uminho.pt

Featured Application: This paper presents a numerical methodology for the hygro-thermo-mechanical analysis of masonry structures. The proposed approach can be used to evaluate the hygro-thermal performance of masonry walls as well as to complement the structural assessment considering other static or dynamic loads. The methodology can be further extended to include durability and aging aspects, and to study the compatibility between masonry units and mortars.

Abstract: Masonry walls comprise an important part of the building envelope and, thus, are exposed to environmental effects such as temperature and moisture variations. However, structural assessment usually neglects the influence of these hygro-thermal loads and assumes ideal conditions. This paper presents a hygro-thermo-mechanical model and its application to simulate the impact of temperature- and moisture-related phenomena on the structural behavior of masonry walls. A fully coupled heat and mass transfer model is presented and a 2D finite element model is prepared to simulate the behavior of a brick masonry wall under various hygro-thermal scenarios. Two different mortars are considered: namely, cement mortar and natural hydraulic lime mortar. The results are evaluated in terms of temperature and moisture content distribution across the wall thickness. The hygro-thermal model is further extended to incorporate mechanical effects through the total strain additive decomposition principle. It is shown that the hygro-thermo-mechanical response of the brick masonry wall is a complex 2D phenomenon. Moreover, the environmental loads change the natural stress distribution caused by gravitational loads alone. Finally, the wall with cement mortar develops higher levels of stress when compared to the one with lime mortar, due to the dissimilar hygro-thermal behavior between the constituent materials.

Keywords: masonry; fired-clay brick; cement mortar; natural hydraulic lime mortar; multi-layered material; heat and mass transfer; multi-physics model; environmental loads; hygro-thermal stress; hygro-thermo-mechanical analysis

Citation: Ramirez, R.; Ghiassi, B.; Pineda, P.; Lourenço, P.B. Hygro-Thermo-Mechanical Analysis of Brick Masonry Walls Subjected to Environmental Actions. *Appl. Sci.* **2023**, *13*, 4514. https://doi.org/10.3390/app13074514

Academic Editors: Angelo Luongo and Simona Di Nino

Received: 5 March 2023
Revised: 29 March 2023
Accepted: 29 March 2023
Published: 2 April 2023

1. Introduction

Ancient and contemporary buildings use masonry as one of the most common construction materials for both structural and non-structural applications. As an integral part of the building envelope, masonry walls are exposed to environmental actions, such as direct solar radiation, wind-driven rain, thermal and hygric variations, moisture condensation, and rising damp. The continuous exposure to environmental loads affects the mechanical response of the material and leads to long-term weathering and degradation, e.g., strength loss, damage (cracks) due to induced dimensional changes and internal stresses, and spalling caused by salt crystallization and freeze-thaw [1,2]. The mechanical behavior of masonry structures has been well-documented in the literature under both

static and dynamic loading scenarios [3–5]. However, the structural assessment usually neglects the influence of hygro-thermal loads and assumes ideal conditions. As a result, there is still a limited understanding of the hygro-thermo-mechanical (HTM) behavior of masonry.

For the analysis of coupled hygro-thermal phenomena in masonry structures, it is necessary to first define a multi-physics model to describe heat and mass transfer in porous materials and multi-layered components. Several hygro-thermal models for porous building materials are available in the literature, e.g., [6–8]. Their application to multi-layered cases, however, demands specific requirements: namely, the need to use a driving potential continuous across the interfaces or the consideration of interfacial effects on the heat and mass transfer mechanisms. Perfect contact is usually assumed for heat conduction through the interface. Consequently, the hygro-thermal models commonly disregard interfacial effects on heat transfer. On the other hand, the simulation of moisture transport in multi-layered cases still presents some challenges. Only a few investigations have focused on interface modeling for mass transfer problems in masonry, e.g., [9–12], and a unified methodology to characterize the effect of brick–mortar interfaces has not been achieved yet. Vereecken and Roels [13] proved that masonry can be modeled as a homogeneous continuum with brick properties to simulate certain water absorption scenarios. Other authors have employed a similar approach for one-dimensional (1D) simulations, e.g., [14,15]. Conversely, for two-dimensional (2D) analyses, the most common approach is still the differentiation of brick units and mortar joints, although the interfacial effects are usually neglected [14,16,17]. Nonetheless, several experimental studies have proven the impact of interfaces on water absorption in masonry [9–12,18]. Thus, further research on the modeling of hydraulic interfaces is required.

Most of the scientific advances in heat and mass transfer in porous building materials have come from the disciplines of Material Sciences and Building Physics. In this context, the improvement of hygro-thermal models and the development of new numerical tools have allowed for more complex and detailed hygro-thermal simulations. Nonetheless, the link between the heat and moisture fields and solid mechanics has not been exploited yet. On one hand, experimental studies on structural elements are normally conducted under controlled, standard laboratory conditions. On the other hand, numerical simulations usually neglect the influence of hygro-thermal loads and assume ideal conditions. The study of HTM effects has received more attention in concrete structures, e.g., curing of concrete for application in dams [19,20]. For masonry, some research has been devoted to the mechanical behavior of walls under extreme scenarios such as high temperatures during fire, e.g., [21,22]. However, the influence of temperature and moisture actions caused by normal environmental conditions are usually disregarded and so are the hygro-thermally induced stresses. To date, few studies have approached the mechanical response of masonry as affected by this type of environmental conditions, e.g., [23–25].

Ramézani and Jeong [24] developed a one-way coupled HTM model to analyze the behavior of a limestone masonry wall subjected to environmental loads. The authors created a 2D finite element model and performed a series of non-isothermal, non-isohygral, steady-state analyses while isolating and combining the different physics. From a comparison between the mechanical, thermo-mechanical, and HTM results, they were able to identify the contribution of each field to the overall response. Moreover, it was shown that the distribution of stresses in the wall was geometry-dependent, and the highest tensile values were concentrated in the vertical head joints and the corners of the masonry units. Transient analyses were also performed to analyze the evolution of the moisture and temperature distributions from the initial condition to the steady-state equilibrium. The authors did not perform transient HTM analyses for variable environmental conditions and this type of analysis is still missing in the literature.

Some authors have dealt with independent thermo-mechanical or hygro-mechanical problems in masonry. For the former, most research is devoted to the mechanical response of structural elements under high-temperature conditions. Among the hygro-mechanical

studies, Castellazzi et al. [16] developed a multi-scale numerical framework for the analysis of masonry walls subjected to water absorption, e.g., rising damp. In particular, the authors employed a two-dimensional discrete coupled hygro-mechanical model to assess the influence of the moisture field on the structural response as well as to incorporate the effect of mechanical degradation on the moisture transport process. In line with the hygro-mechanical studies, research on salt transport and crystallization in porous materials has received more attention in recent years, e.g., [25–31]. The proposed models have been proved able to predict the transport of salts and subsequent crystallization under different environmental scenarios. An all-encompassing analysis considering the additive effects of thermal dilation, hygric swelling, and crystallization pressure is still missing.

On the other hand, scientific works on fully coupled HTM problems in masonry are notably scarce. Regarding this aspect, further investigation is needed to determine the influence of moisture on the mechanical performance of the material, including linear and non-linear behavior as well as damage. Similarly, more research is necessary to quantify and reproduce the reverse coupling, that is, the mechanical effects (stress variation, creep, volumetric changes, damage, cracking) on moisture transport. The studies developed by Mertens [32] and Carmeliet [33] are worth mentioning, and they focused on the non-linear hysteretic behavior of quasi-brittle porous materials.

Different finite element computational strategies have been developed for the mechanical analysis of masonry: namely, micro- and macro-modeling approaches [34]. These strategies can be further extended to hygro-thermal analyses as presented in Figure 1. In the case of micro-modeling, which is the focus of this work, the constituent materials (brick units and mortar) and brick–mortar interfaces are modeled separately. On the other hand, macro-modeling approaches assume a homogenized continuum material.

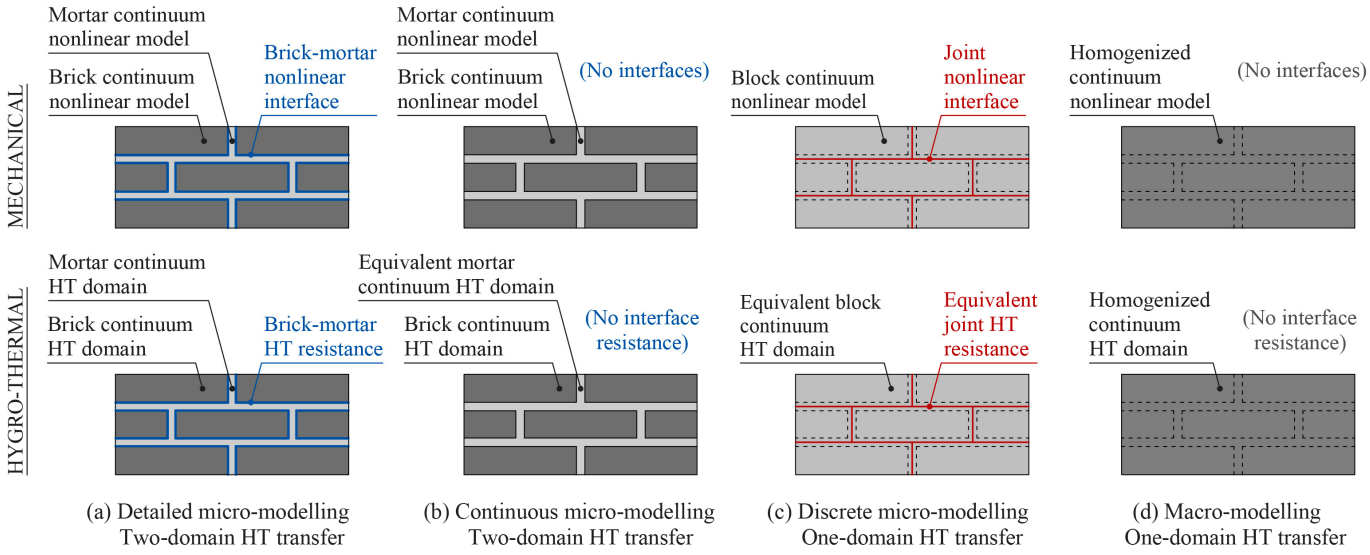

Figure 1. Modeling strategies for masonry. Adapted from [35], following [34,36].

This paper presents a hygro-thermo-mechanical (HTM) model to simulate the impact of hygro-thermal loads on the structural response of masonry walls. Moreover, this paper provides a new insight into the HTM behavior of masonry when subjected to normal environmental actions, considering both constant and variable temperature and relative humidity conditions. These aspects are usually disregarded in experimental and simulation works, and therefore, there is an evident lack of scientific knowledge. This paper is structured as follows. First, a fully coupled heat and moisture transport model is proposed and hygro-thermal simulations are performed using a 2D finite element model of a three-wythe brick wall. The results of the hygro-thermal studies are evaluated in terms of temperature and relative humidity profiles across the thickness of the wall as well as for

different points on the external and internal surfaces. The evolution of temperature and relative humidity obtained by transient analyses show that heat transfer is significantly faster than moisture transport. Subsequently, the analyses were extended to incorporate mechanical effects by the use of a one-way HTM model. For all the analyses, two different mortars were considered for the wall: namely, natural hydraulic lime and cement mortar. It is proven that the wall with cement mortar develops higher stresses when compared to the one with lime mortar, due to the dissimilar hygro-thermal behavior between the constituent materials. Moreover, the results show that the HTM response of masonry walls is a complex 2D phenomenon. Finally, the environmental loads change the natural stress distribution caused by gravitational loads alone and induce localized concentrations of compressive and tensile stresses.

2. Hygro-Thermal Model

This section describes the numerical model adopted for hygro-thermal simulations. The moisture transport model was validated by the authors in [37]. In the present paper, this model is extended to incorporate the thermal field. Thus, the theoretical bases and main assumptions of the extended model are briefly presented here.

Masonry is described as a porous medium made up of a matrix of interconnected pores inside a solid skeleton. The solid phase is assumed continuous, homogeneous, inert (no chemical reactions), isotropic, and non-deformable. Moreover, pores are assumed cylindrical, with a homogeneous, isotropic distribution inside the material. The void space defined by the pore system is filled with a liquid and a gaseous phase in different proportions. The liquid phase is pure and incompressible, whereas the air phase is an ideal mixture of dry air and water vapor at atmospheric pressure. For simplicity, advective air flow is not implemented in the model and pressure gradients are considered negligible. Additionally, a local instantaneous thermodynamic equilibrium is assumed between the liquid and gaseous phases. Consequently, the contributions of liquid water and water vapor may be combined to define a global moisture content. Nonetheless, the contribution of water vapor to the total moisture content is negligible. Knudsen flow is not considered, and the effect of gravity is neglected since capillary forces are dominant.

The volume fraction of (moist) air inside the porous space does not contribute to the overall thermal conductivity and specific heat capacity of the material. The formation of ice is out of the scope of the present work; thus, the temperature remains above the freezing point of water. Heat flux induced by moisture transport (Dufour effect) as well as moisture flux induced by temperature gradients (Soret effect) are considered negligible. The coupling between heat and moisture fields will be further discussed in the following sections.

The effect of imperfect contact interfaces in multi-layered cases is considered for moisture transport by means of hydraulic resistances [9]. For heat transfer, the impact of interfaces between adjacent materials is disregarded so that the temperature profiles are continuous between layers.

2.1. Governing Equations

The heat transfer model considers conductive heat transfer according to Fourier's Law and accounts for the heat of vaporization:

$$\rho C \frac{\partial T}{\partial t} = \nabla \cdot (\lambda \nabla T) + L_v \nabla \cdot \left[\frac{\delta_a}{\mu} \nabla (\varphi p_{v,sat}) \right], \quad (1)$$

where ρC [J/(m^3·K)] is the volumetric heat capacity at constant pressure, T [K] is the temperature, t [s] is time, λ [W/(m·K)] is the thermal conductivity, L_v [J/kg] is the latent heat of evaporation, δ_a [kg/(m·s·Pa)] is the water vapor permeability of still air, μ [–] is the water vapor resistance of the material, φ [–] is the relative humidity, and $p_{v,sat}$ [Pa] is the vapor saturation pressure. The second term on the right-hand side of Equation (1) represents the latent heat of vaporization associated with liquid/gas phase change.

On the other hand, the multi-phase moisture transport model stems from Fick's laws of diffusion and considers a combination of liquid transport by capillarity and vapor diffusion:

$$\frac{\partial w}{\partial \varphi}\frac{\partial \varphi}{\partial t} = \nabla\cdot\left(\frac{\partial w}{\partial \varphi}D_w\nabla\varphi\right) + \nabla\cdot\left[\frac{\delta_a}{\mu}\nabla(\varphi p_{v,sat})\right], \quad (2)$$

where w [kg/m^3] is the moisture content, and D_w [m^2/s] is the liquid water diffusivity. The modified version of the exponential expression proposed by Künzel [38] is used to describe the liquid water diffusivity:

$$D_w = \gamma\cdot\left(\frac{A_w}{w_{cap}}\right)^2\cdot 10^{3\cdot\left(\frac{w}{w_{cap}}-1\right)}, \quad (3)$$

where γ [–] is a diffusivity factor depending on the material and transport process (wetting/drying), A_w [kg/(m^2·s$^{0.5}$)] is the capillary absorption coefficient, and w_{cap} [kg/m^3] is the capillary moisture content.

2.2. Interface Modeling

The brick–mortar interfaces are assumed to have an imperfect contact for moisture transport. Therefore, the moisture flow across the interface, g_{IF} [kg/(m^2·s)], is modeled through the introduction of an interface permeability, K_{IF} [s/m], or an interface resistance R_{IF} [m/s], such as [9]:

$$g_{IF} = K_{IF}\frac{\partial p_c}{\partial x} = \frac{1}{\frac{1}{K_{IF}}}\frac{\partial p_c}{\partial x} = \frac{\Delta p_c}{\frac{1}{K_{IF}}\Delta x} = \frac{\Delta p_c}{R_{IF}}, \quad (4)$$

where p_c [Pa] is the capillary pressure, which can be related to the relative humidity using Kelvin's equation:

$$p_c = \rho_w\cdot R_v\cdot T\cdot\ln\varphi, \quad (5)$$

with ρ_w [kg/m^3] being the density of water, and R_v [J/(kg·K)] being the universal gas constant for water vapor.

Thus, assuming the applicability of Kelvin's equation, the moisture flow across the interface can be defined as:

$$g_{IF} = K_{IF}\frac{\partial p_c}{\partial \varphi}\frac{\partial \varphi}{\partial x} = K_{IF}\frac{\rho_w\cdot R_v\cdot T}{\varphi}\frac{\partial \varphi}{\partial x} = \frac{\rho_w\cdot R_v\cdot T}{\varphi}\frac{\Delta\varphi}{\frac{1}{K_{IF}}\Delta x} = \frac{\rho_w\cdot R_v\cdot T}{\varphi}\frac{\Delta\varphi}{R_{IF}}. \quad (6)$$

2.3. Hygro-Thermal Coupling

Simultaneous heat and mass transfer in porous media constitutes a highly coupled problem: that is, temperature balance and thermal properties vary according to moisture content, while the moisture-related properties and moisture equilibrium are dependent on temperature.

2.3.1. Moisture Dependency of Thermal Parameters

It is known that the heat capacity of a porous material is directly related to its moisture content. In particular, if the material is wet, the effect of moisture on heat capacity can be considered using:

$$\rho C = \rho_{bulk}C_p + w\cdot C_w, \quad (7)$$

where ρ_{bulk} [kg/m^3] is the bulk density of the material, C_p [J/(kg·K)] is the specific heat capacity of the dry material, and C_w [J/(kg·K)] is the specific heat capacity of liquid water. The specific heat capacity of water has a weak thermal dependence for the range of temperatures of interest in the present study [39]. Therefore, it is taken as a constant, $C_w = 4182$ J/(kg·K), which corresponds to the specific heat capacity of water at 20 °C.

Additionally, the moisture influence on the thermal conductivity of a wet porous material can be determined through the following expression:

$$\lambda = \lambda_0(1 + b{\cdot}w/\rho_{bulk}) = \lambda_0\left(1 + b{\cdot}w_g\right), \tag{8}$$

where λ_0 [W/(m·K)] is the thermal conductivity of the solid matrix, and b [–] is a material-dependent thermal conductivity supplement. The supplement b can be described as the fractional increase (sometimes expressed as a percentage) of the thermal conductivity per mass-percent moisture content, i.e., moisture mass per unit mass of dry material × 100. Thermal conductivity has a minor dependence on temperature for normal environmental conditions, and therefore, its thermal dependency is disregarded [40].

For practical applications, the thermal conductivity of porous materials is often given as a linear relationship based on experimental values determined for different moisture content conditions. For instance, an expression of the form $\lambda = A + B{\cdot}w$ has been extensively used in the literature to describe the thermal conductivity of brick [41–43]. In the previous expression, the intercept $\lambda(w = 0)$ stands for the thermal conductivity of the dry material, λ_0. In turn, the slope of the curve represents the increase in thermal conductivity per moisture content, and according to Equation (8), it must be equal to $\lambda_0{\cdot}b/\rho_{bulk}$.

2.3.2. Temperature Dependency of Hygric Parameters

The coefficient of thermal expansion of most building materials lies in the order of 10^{-5} to 10^{-6} °C^{-1} for normal temperatures. As a result, any volumetric change induced by temperature variations within the normal temperature range falls outside ordinary measurement capabilities [44]. Thus, it is generally accepted that open porosity, ϕ_o [–], and bulk density, ρ_{bulk} [kg/m^3], can be considered as constant for the range of temperatures of interest in this study [45]. Moreover, once the volumetric variation of the porous solid matrix is disregarded, the influence of temperature on the saturation moisture content, w_{sat} [kg/m^3], stems solely from the water density, which has a weak dependency on temperature with less than a 1.20% decline between 0 °C and 50 °C [46]. As a result, w_{sat} [kg/m^3] can be considered as a constant independent of temperature. Here, an analogous logic is followed for the definition of the capillary moisture content, w_{cap} [kg/m^3], which is considered constant. However, it must be noted that a widely accepted theory to describe the relationship between w_{cap} and temperature is still lacking in the literature.

Apart from the saturation state boundaries, w_{cap} and w_{sat}, the equilibrium moisture content of unsaturated porous materials is dependent on the temperature. The thermal dependency of moisture storage implies a shift in the moisture storage function (sorption isotherm or water retention curve). This behavior is expected since higher temperatures are associated with higher energy levels, which cause faster transport and release of water molecules [47]. For this reason, both adsorption and desorption curves corresponding to higher temperatures lie below the 'colder' isotherms [48]. The thermal dependency of moisture storage can be expressed analytically through temperature-dependent fitting parameters. As an example, Castellazzi et al. [49] proposed the following expression:

$$w(\varphi) = w_{cap}{\cdot}\frac{\psi(T) - 1}{\psi(T) - \varphi}{\cdot}\varphi, \tag{9}$$

where $\psi(T)$ [–] is a fitting parameter dependent on temperature. It is noted that ψ is inversely proportional to the temperature. The correlation between ψ and T must be established from experimental data. However, the influence of temperature on moisture storage has not been sufficiently studied and experimental data are scarce. The available information suggests a negligible temperature dependency for barely hygroscopic materials, such as fired-clay brick [44]. For the sake of simplicity, the thermal effects on moisture storage are not considered in the simulations presented in this paper.

The influence of temperature on vapor diffusion is partly considered through the water vapor permeability of still air, δ_a [kg/(m·s·Pa)], defined empirically as [50]:

$$\delta_a = \frac{2.31 \cdot 10^{-5}}{R_v \cdot T} \frac{p_0}{p} \left(\frac{T}{273.15} \right)^{1.81}, \quad (10)$$

where $p_0 = 101{,}325$ Pa is the standard atmospheric pressure, and p [Pa] is the ambient barometric pressure.

Additionally, the saturation vapor pressure, $p_{v,sat}$ [Pa], is a non-linear function of temperature defined empirically as [51,52]:

$$p_{v,sat} = 610.7[\text{Pa}] \cdot 10^{7.5\left(\frac{T-273.15}{T-35.85}\right)}. \quad (11)$$

The impact of temperature on the liquid transport term has been studied by different authors: in particular, its effect on the water absorption coefficient, A_w [kg/(m^2·s$^{0.5}$)], or sorptivity, $S = A_w/\rho_w$ [m/s$^{0.5}$], e.g., [44,53–56]. The reported results support the validity of the Lucas–Washburn law, which describes the water penetration depth x [m] after a period of time t [s] as [57]:

$$x = \sqrt{\frac{\sigma r \cos\theta}{2\eta}} \cdot \sqrt{t}, \quad (12)$$

where σ [N/m] is the surface tension of water, r [m] is the equivalent hydraulic capillary radius, θ is the contact angle, and η [Pa·s] is the viscosity of water. This expression states that liquid water flow is influenced by a series of factors. In order to understand how the overall liquid flow is affected by variations of temperature, it is convenient to study the impact of temperature on each of those factors separately. First, assuming that the porous structure undergoes negligible changes due to thermal (or hygric) expansion, it is reasonable to assume a constant r. Moreover, temperature has only a slight impact on the contact angle θ, so its influence can be disregarded. Therefore, the remaining temperature-dependent parameters are the surface tension σ and the viscosity η. Comparing the definition of the capillary absorption coefficient with the Lucas–Washburn equation, it is possible to establish a relation of proportionality as suggested by Gummerson et al. [53]:

$$A_w \propto \sqrt{\sigma/\eta}. \quad (13)$$

Considering the previous relation, Feng and Janssen [44] fitted tabulated values for σ and η (temperatures between 0 °C and 50 °C) and established a linear model to describe the relationship between A_w and T:

$$A_w = k\sqrt{\sigma/\eta} = k[0.095(T - 273.15) + 6.566], \quad (14)$$

where k [kg/m$^{2.5}$] is a micro-structure-dependent but temperature-independent factor. As an example, these authors studied the absorption behavior of different building materials under several temperature conditions and determined $k = 0.0059$ for brick ($A_w = 0.052$ at 22.5 °C). For cement mortars, Hanumanthu and Sarkar [56] found $k = 0.0019$–0.0023 ($A_w = 0.016$–0.020 at 20 °C), whereas for NHL mortar, the data presented by Karagiannis et al. [58] were reinterpreted by Feng and Janssen [55], who established $k = 0.0125$ ($A_w = 0.106$ at 20 °C).

2.4. Initial and Boundary Conditions

The hygro-thermal model is completed by introducing initial and boundary conditions. The Dirichlet boundary condition yields:

$$T = \bar{T}, \quad (15)$$

$$\varphi = \bar{\varphi}, \tag{16}$$

where $\bar{T}$ [K] and $\bar{\varphi}$ [–] are the prescribed temperature and relative humidity at the boundary, respectively.

Conversely, the Neumann boundary condition is defined as a flux derived from a temperature or vapor pressure difference:

$$q = h_T(T_{ext} - T), \tag{17}$$

$$g = h_m(p_{v,ext} - p_v), \tag{18}$$

where q [W/m^2] is the convective heat flux, h_T [W/(m^2·K)] is the heat transfer coefficient, T_{ext} [K] is the temperature of the environment, T [K] is the temperature at the boundary, g [kg/(m^2·s)] is the convective moisture flux, h_m [s/m] is the convective mass transfer coefficient, and $p_{v,ext}$ [Pa] and p_v [Pa] are the partial vapor pressures defined for the environment and at the boundary, respectively. In the present work, h_T accounts for the combined effects of convection and long-wave radiation exchanges with the environment. Thus, this lumped convective/radiative heat transfer coefficient is defined as

$$h_T = h_{T,c} + h_{T,r}, \tag{19}$$

where $h_{T,c}$ [W/(m^2·K)] is the convective heat transfer coefficient, and $h_{T,r}$ [W/(m^2·K)] is the radiative heat transfer coefficient. The heat transfer coefficient is dependent on the local air flow conditions, the temperature, the geometry, and the orientation of the studied element, which makes an accurate estimation very complex. For building applications, a simplified approach is usually adopted, and the heat transfer coefficient is assumed to be constant [38].

3. Hygro-Thermal Simulations and Discussion

The model described in the previous section is used here to simulate the hygro-thermal behavior of a brick masonry wall. First, the main features of the numerical model are described: geometry, material properties, and boundary conditions. Then, two sets of analyses are performed: namely, steady-state and time-dependent analyses. Finally, the results of the simulations are presented in terms of temperature and relative humidity profiles, and the obtained trends are discussed. The analyses described in the following paragraphs are based on the finite element method and were performed using the software COMSOL Multiphysics [59].

3.1. Description of the Numerical Model

A common type of load-bearing masonry wall was selected as a case study to perform the hygro-thermal simulations. In particular, the chosen wall is made up of bricks with dimensions 205 mm × 95 mm × 50 mm, and mortar joints 15 mm thick. The resulting structure is a 315 mm thick (three-wythe brick) masonry wall with a total height of 2650 mm. The geometrical configuration of the wall is depicted in Figure 2. The described geometry was used to prepare a two-dimensional (2D) model.

The material properties used for the hygro-thermal simulations are presented in Table 1. Two types of mortar were considered for the analyses: namely, natural hydraulic lime mortar (LM) and cement mortar (CM). Moreover, the brick–mortar interfaces were assumed to have perfect contact for heat transfer, whereas imperfect contact was considered for moisture transport. Thus, a hydraulic resistance $R_{IF} = 2.0 \times 10^9$ m/s was assigned to the brick–mortar interfaces.

The wall is assumed to be located in Guimarães (Portugal), which has an annual average temperature $\vartheta = 13.5$ °C and an annual average relative humidity RH = 74% [60]. Additionally, the wall is considered to have initial conditions equal to these yearly average

values; thus, $\vartheta = 13.5$ °C and $\varphi_0 = 0.74$. One face of the wall is exposed to the exterior, whereas the opposite face is in contact with a conditioned interior space with constant temperature and relative humidity: namely, 20 °C and 50% RH. It must be noted that the presented configuration is rather unusual for a building envelope in contact with a modern habitable interior space since it lacks any type of dedicated moisture barrier or thermal insulation. Nonetheless, this configuration is reasonable for certain historical walls and expedient for the analyses at hand, in which thermal and moisture gradients are of interest. In the case of a masonry wall with good insulation on the interior side, adiabatic boundary conditions could be assumed for the internal face.

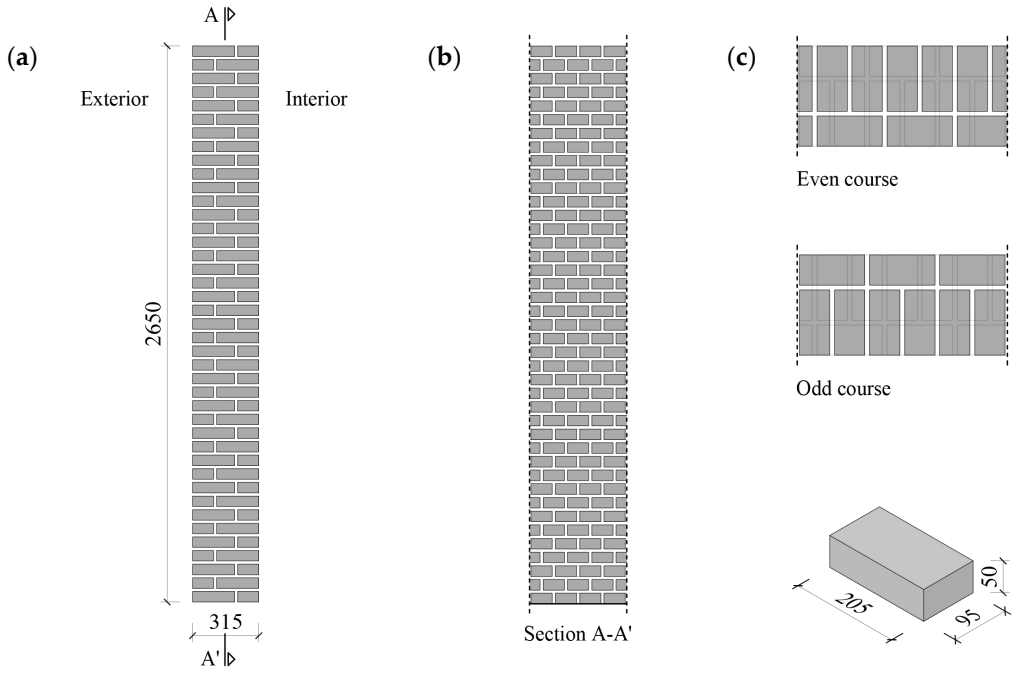

Figure 2. Schematic geometrical configuration of the brick masonry wall: (**a**) transversal cross-section; (**b**) vertical cross-section; (**c**) bond arrangement and geometry of the brick units. Dimensions in mm.

The hygro-thermal simulations were performed through both steady-state (SS) and time-dependent (TD) analyses. The SS analysis was used to evaluate the final hygro-thermal equilibrium attained by the wall considering constant environmental conditions as explained in the previous paragraph. Moreover, two sets of time-dependent analyses were defined. In particular, TD1 was performed to evaluate the evolution of temperature and relative humidity profiles across the wall from the initial state to hygro-thermal equilibrium with the environment. Therefore, the final stage of TD1 is analogous to the results obtained with the stationary analysis SS. Additionally, the transient study TD2 considered the wall already in equilibrium with the environment (the initial conditions were taken from the results of SS or the final stage of TD1) and then imposed variable external conditions. In particular, the external conditions for TD2 were assumed to vary with time following a sinusoidal law, given by:

$$\vartheta(t) = 13.5 + 10 \cdot \cos(2\pi t - \pi/2), \tag{20}$$

$$\varphi(t) = 0.74 + 0.12 \cdot \cos(2\pi t + \pi/2), \tag{21}$$

for the external temperature and relative humidity, respectively, with t expressed in days. The proposed thermal variation corresponds to the average maximum temperature excursion that can be experienced in a single day during mid-season periods, i.e., $\Delta\vartheta \approx 20$ °C. Additionally, average values of the seasonal relative humidity were selected to determine

the range of daily moisture variation, and the corresponding sinusoidal function was set to follow an opposite trend to the one defined for the temperature.

The initial and boundary conditions used for the hygro-thermal simulations of the masonry wall are summarized in Table 2. Neumann boundary conditions were imposed on the external and internal faces of the wall. Therefore, heat and moisture fluxes were defined with commonly accepted values for the convective transfer coefficients. In particular, heat transfer coefficients $h_{T,ext} = 25$ W/(m^2·K) and $h_{T,int} = 8$ W/(m^2·K) were imposed at the external and internal faces, respectively [61]. It is noted that the heat transfer coefficient selected for the external surface already takes into account the radiative contribution. Furthermore, convective mass transfer coefficients $h_{m,ext} = 2.0 \times 10^{-7}$ s/m and $h_{m,int} = 3.0 \times 10^{-8}$ s/m were considered for the external and the internal faces of the wall, respectively [61].

Table 1. Summary of material properties used for the hygro-thermal simulations.

Material	Property	Symbol	Value	Units	Source
Brick	Bulk density	ρ_{bulk}	1900	kg/m^3	Ramirez et al. [18]
	Open porosity	ϕ_o	0.280	–	
	Capillary moisture content	w_{cap}	240	kg/m^3	
	Fitting parameter for sorption isotherm	ψ	1.0070	–	
	Water absorption coefficient (∥ bed face)	$A_{w,\parallel}$	0.104	kg/(m^2·s$^{0.5}$)	
	Water absorption coefficient (⊥ bed face)	$A_{w,\perp}$	0.075	kg/(m^2·s$^{0.5}$)	
	Water vapor resistance factor	μ	34.14	–	
	Specific heat capacity	C_p	825	J/(kg·K)	Koci et al. [62]
	Thermal conductivity	λ_0	0.59	W/(m·K)	
	Thermal conductivity supplement	b	12.74	–	
Lime mortar (LM)	Bulk density	ρ_{bulk}	2060	kg/m^3	Ramirez et al. [18]
	Open porosity	ϕ_o	0.230	–	
	Capillary moisture content	w_{cap}	190	kg/m^3	
	Fitting parameters for adsorption isotherm	a_{ads}	3.80×10^{-6}	1/Pa	
		m_{ads}	0.352	–	
	Fitting parameters for desorption isotherm	a_{des}	1.19×10^{-5}	1/Pa	
		m_{des}	0.235	–	
	Water absorption coefficient (isotropic)	$A_{w,ISO}$	0.080	kg/(m^2·s$^{0.5}$)	
	Water vapor resistance factor	μ	15.00	–	Prangnell [63]
	Specific heat capacity	C_p	840	J/(kg·K)	Kumaran [64]
	Thermal conductivity	λ_0	0.85	W/(m·K)	
	Thermal conductivity supplement	b	9.53	–	
Cement mortar (CM)	Bulk density	ρ_{bulk}	2000	kg/m^3	Ramirez et al. [18]
	Open porosity	ϕ_o	0.210	–	
	Capillary moisture content	w_{cap}	180	kg/m^3	
	Fitting parameters for adsorption isotherm	a_{ads}	1.43×10^{-6}	1/Pa	
		m_{ads}	0.285	–	
	Fitting parameters for desorption isotherm	a_{des}	2.51×10^{-5}	1/Pa	
		m_{des}	0.213	–	
	Water absorption coefficient (isotropic)	$A_{w,ISO}$	0.060	kg/(m^2·s$^{0.5}$)	
	Water vapor resistance factor	μ	25.00	–	Prangnell [63]
	Specific heat capacity	C_p	932	J/(kg·K)	Kumaran [64]
	Thermal conductivity	λ_0	1.72	W/(m·K)	
	Thermal conductivity supplement	b	9.29	–	

Two-dimensional quadrilateral elements with quadratic shape functions were used for the discretization of the models. After preliminary sensitivity analyses to determine the optimal mesh size, the average element size was set to 5 mm. The primary variables, namely, temperature and relative humidity, were interpolated based on standard Lagrangian shape

functions. Moreover, the backward finite difference method was used for automatic time discretization during the transient analyses. Finally, an iterative procedure based on the Newton–Raphson method was applied to solve the non-linear differential equations. It is noted that the finite element formulations and solution algorithms were implemented using the existing codes in COMSOL Multiphysics [59].

Table 2. Summary of the initial and boundary conditions used for the hygro-thermal simulations.

Analysis	Initial Conditions		Exterior Boundary Conditions				Interior Boundary Conditions			
	ϑ_0 [°C]	φ_0 [–]	ϑ_{ext} [°C]	$h_{T,ext}$ [W/(m^2·K)]	φ_{ext} [–]	$h_{m,ext}$ [s/m]	ϑ_{int} [°C]	$h_{T,int}$ [W/(m^2·K)]	φ_{int} [–]	$h_{m,int}$ [s/m]
SS	13.5	0.74	13.5	25	0.74	2.0×10^{-7}	20.0	8	0.50	3.0×10^{-8}
TD1	13.5	0.74	13.5	25	0.74	2.0×10^{-7}	20.0	8	0.50	3.0×10^{-8}
TD2	SS results [1]	SS results [1]	Equation (20)	25	Equation (21)	2.0×10^{-7}	20.0	8	0.50	3.0×10^{-8}

[1] Analogous to the final stage of TD1.

3.2. Hygro-Thermal Behavior of a Brick Masonry Wall

3.2.1. Steady-State Analysis (SS)

The temperature and relative humidity profiles obtained for the steady-state analyses are shown in Figures 3 and 4, respectively. The results show only minor differences between the two studied cases: namely, the wall with lime mortar (LM) and the wall with cement mortar (CM). This was expected considering that the stationary analysis focuses on the final equilibrium state, which is mostly dependent on the external boundary conditions. Moreover, any difference observed in the response of the wall stems from the different behavior of the selected type of mortar, which ultimately accounts for less than 26% of the total cross-sectional area.

It is noted that the temperature and relative humidity values obtained at the external and internal surfaces do not reach the values defined for the boundary conditions: namely, 13.5 °C and 74% RH for the exterior and 20 °C and 50% RH for the interior. This is due to the kind of boundary conditions imposed on the model, i.e., convective flux or Neumann boundary conditions. Therefore, the convective heat transfer and the convective mass transfer coefficients induce, respectively, a temperature and a relative humidity exchange between the environment and the surface of the wall.

Regarding the thermal field (see Figure 3), the temperature profiles for both cases show an overall linear distribution across the thickness of the wall. In a multi-layered material, the transition between adjacent layers with dissimilar thermal conductivity translates into a change of slope in the temperature profile before and after the interface. For the LM case, the presence of mortar joints is barely noticeable since the thermal conductivity properties of bricks and lime mortar are similar. On the contrary, the presence of joints is clearer for the CM case due to the more dissimilar thermal conductivity of bricks and cement mortar. Therefore, for the CM case, it is possible to perceive slight changes in the slope of the temperature profiles at the location of the vertical head joints.

Regarding the hygric response (see Figure 4), the relative humidity profiles for both models show a nearly linear distribution between the two faces of the wall. As was mentioned for the temperature, slight disturbances in the moisture profiles reveal the presence of mortar joints. It is noted that the CM case shows a somewhat less linear trend and slightly higher values of relative humidity across the wall thickness. Moreover, the presence of vertical head joints is clearer for the CM case as well. These aspects can be explained by the marked hygroscopic nature of cement mortar, which contrasts with the less hygroscopic behavior of lime mortar and the barely hygroscopic behavior of bricks.

Considering the results of the hygro-thermal steady-state analysis, rather homogeneous temperature and moisture distributions are obtained for the studied wall configuration. Moreover, the differences between the two types of mortar are not significant. Thus, a macro-modeling approach with equivalent masonry properties could be used instead of the presented detailed micro-modeling. It is recalled that macro-modeling assumes

a homogenized continuum domain, and therefore, implies lesser material and geometrical complexity, with an associated reduction of the computational cost. Furthermore, simplification to a 1D type of analysis would be appropriate as well.

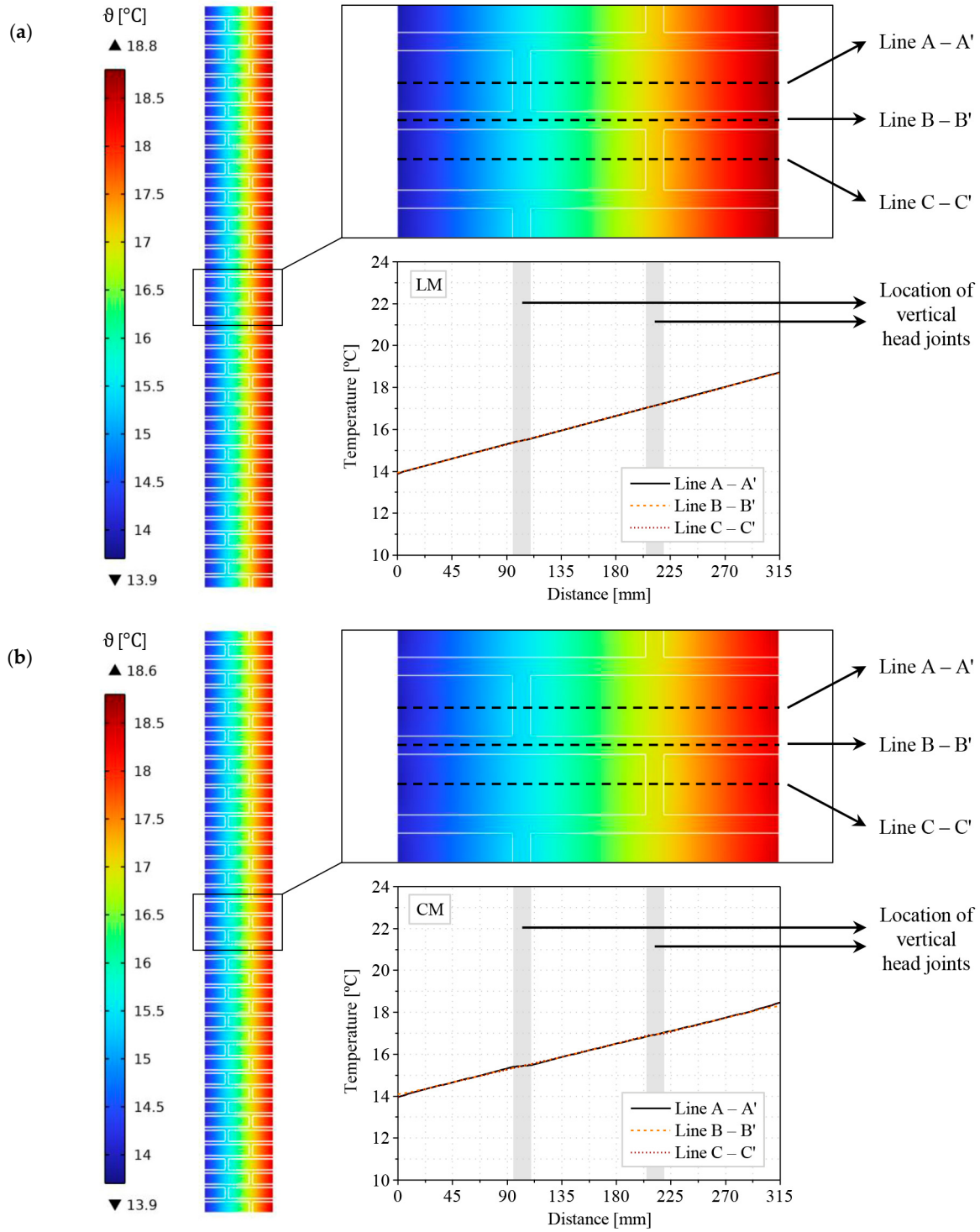

Figure 3. Steady-state analysis (SS). Temperature distribution across the studied three-wythe brick masonry wall: (**a**) joints with lime mortar (LM); (**b**) joints with cement mortar (CM).

3.2.2. Time-Dependent Analysis with Constant Boundary Conditions (TD1)

The previous section dealt with the steady-state equilibrium attained by the studied three-wythe brick masonry wall considering an environment with constant boundary conditions. In this section, the first group of time-dependent analyses, labeled TD1, focuses on the process required for the wall to reach the same state of hygro-thermal equilibrium.

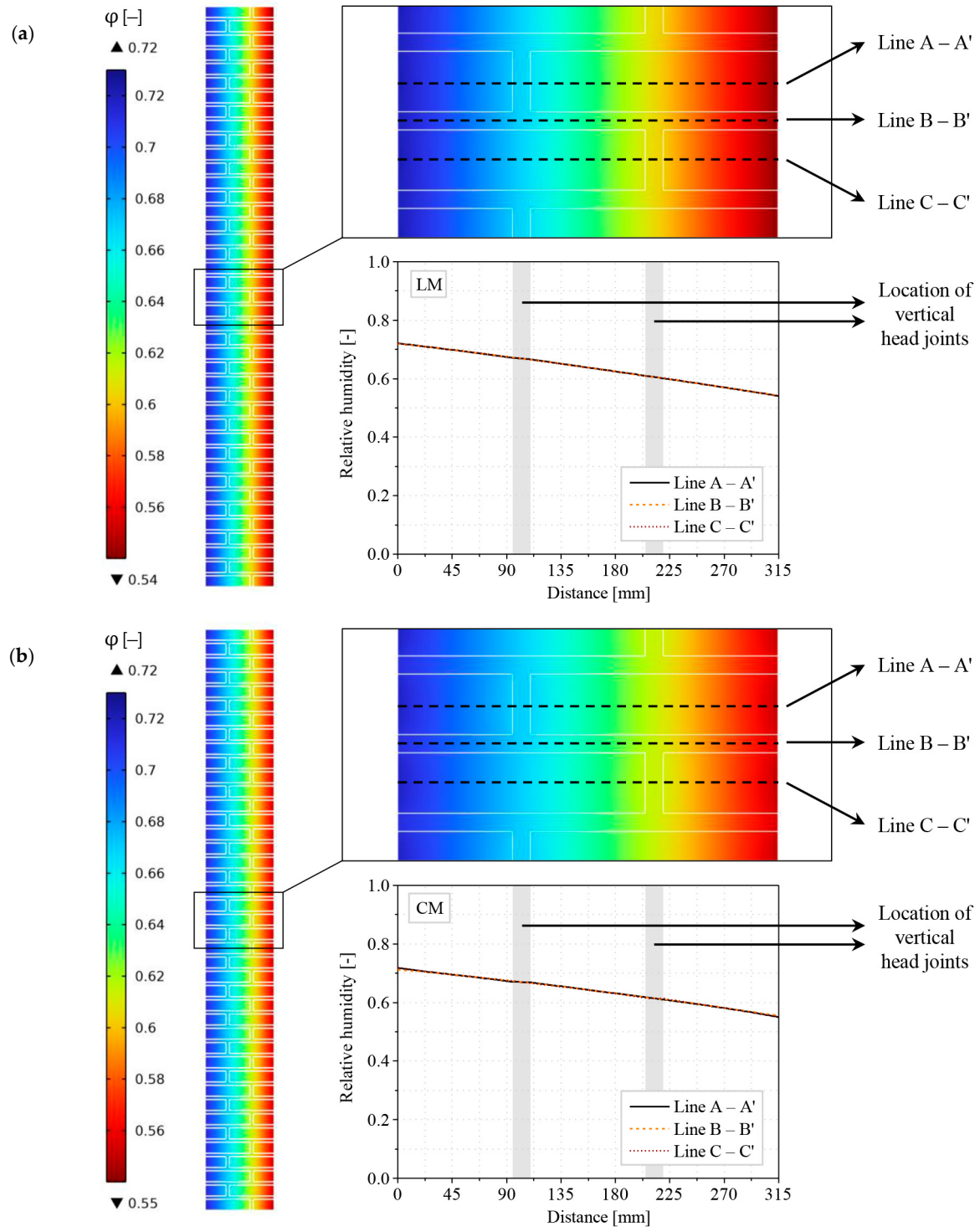

Figure 4. Steady-state analysis (SS). Relative humidity distribution across the studied three-wythe brick masonry wall: (**a**) joints with lime mortar (LM); (**b**) joints with cement mortar (CM).

The evolution of temperature and relative humidity profiles obtained from the TD1 analysis is shown in Figures 5 and 6, respectively. It is worth noting the time difference needed for both processes to reach equilibrium. On one hand, the thermal field attains the steady-state equilibrium in about 60 h. Conversely, moisture transport is a much slower process and hygric equilibrium is only attained after 450 days (or 11,000 h). Taking this into account, heat transfer can be treated as an immediate process in comparison with mass transport. Furthermore, it is possible to conclude that a real structure will not likely attain a full hygric equilibrium considering the usual variability of environmental conditions and the long time required for the materials to accommodate moisture processes.

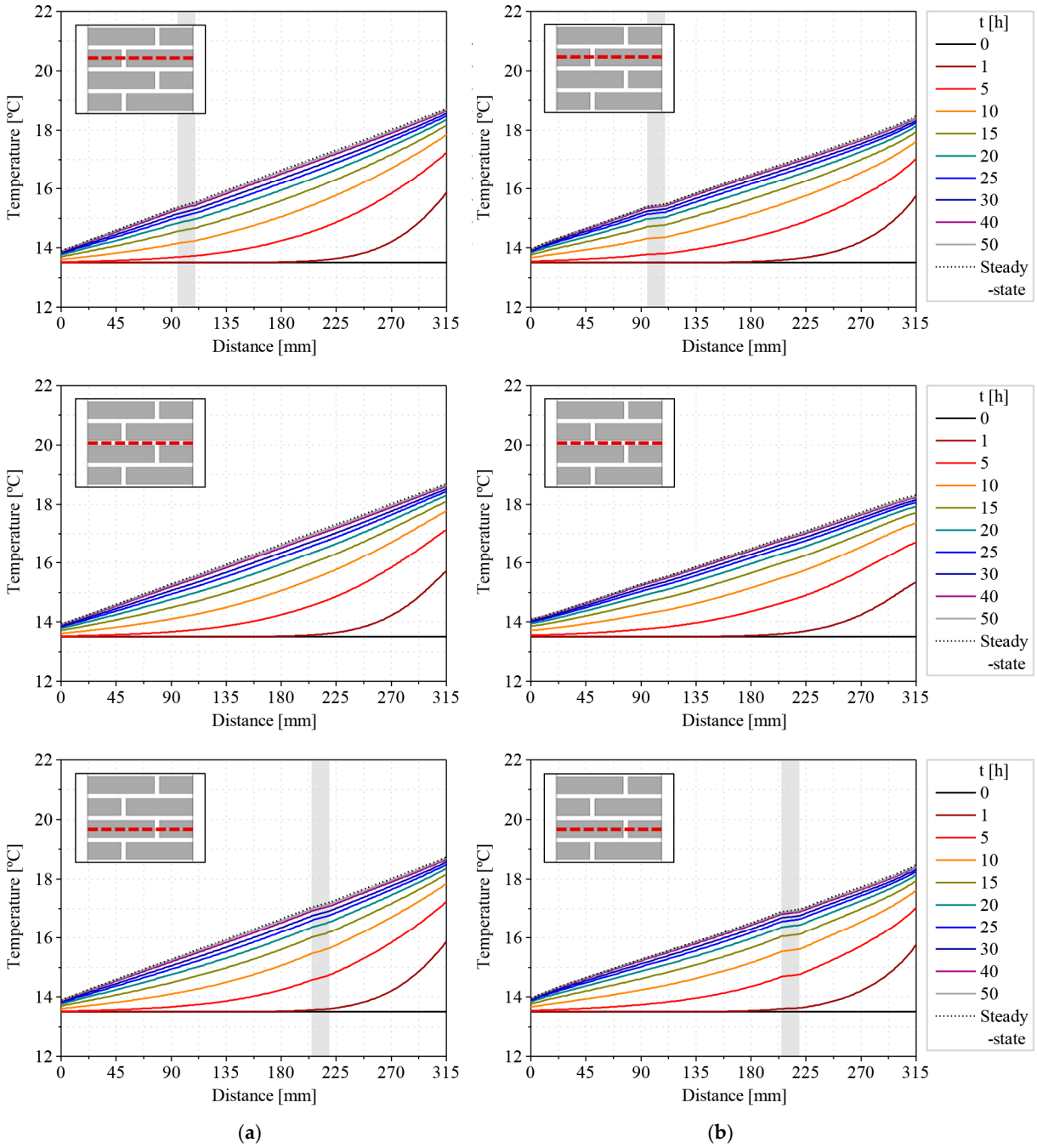

Figure 5. Time-dependent analysis (TD1). Temperature evolution across the studied three-wythe brick masonry wall: (**a**) joints with natural hydraulic lime mortar (LM); (**b**) joints with cement mortar (CM). Lines A–A′ (**top**), B–B′ (**middle**), and C–C′ (**bottom**).

There are some differences between the wall with lime mortar (LM) and the one with cement mortar (CM). On one hand, the temperature evolution is faster for the CM case. In other words, the wall with cement mortar requires less time to reach thermal equilibrium. This is consistent with the higher thermal conductivity of cement mortar in comparison with lime. Conversely, the relative humidity evolution is slower for the CM case. This can be explained by the transport properties as well: cement mortar has lower liquid diffusivity and higher water vapor resistance than its lime counterpart.

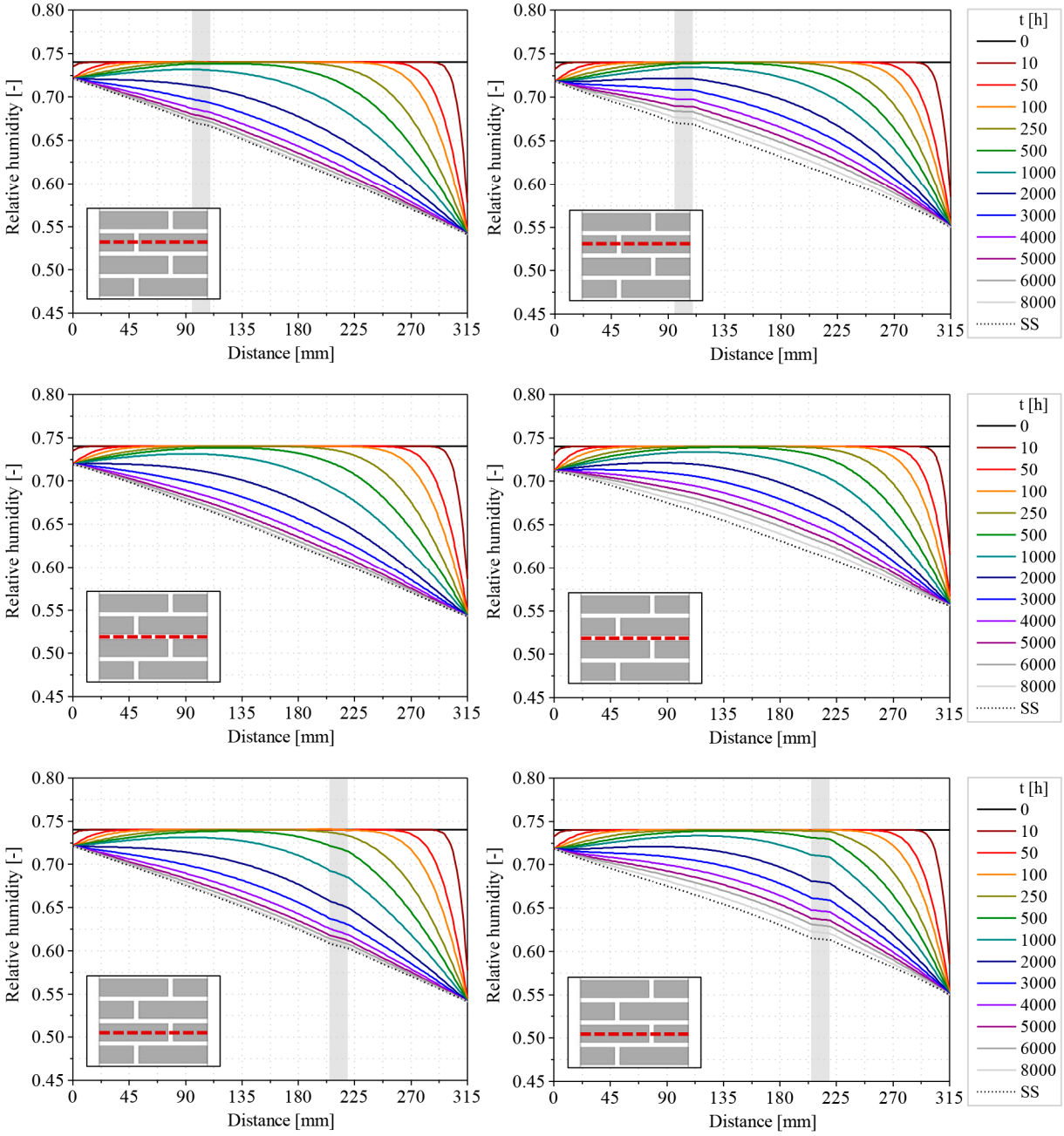

Figure 6. Time-dependent analysis (TD1). Evolution of the relative humidity across the studied three-wythe brick masonry wall: (**a**) joints with natural hydraulic lime mortar (LM); (**b**) joints with cement mortar (CM). Lines A–A′ (**top**), B–B′ (**middle**), and C–C′ (**bottom**).

As was pointed out for the SS analysis, the presence of mortar joints can be distinguished by slope changes in the temperature and relative humidity profiles at the location of the brick–mortar interfaces. It is noted that the TD1 results for the CM case show the location of the vertical head joints more evidently. Once again, this can be explained by the more dissimilar properties between bricks and cement mortar in comparison with lime mortar.

Besides the previous analyses, a parametric study was performed in order to evaluate the influence of the hydraulic resistance on the evolution of relative humidity. In particular, different values of the interface resistance, R_{IF}, were adopted, but the results did not show significant differences. Thus, it was concluded that the impact of the interface resistance was not significant for the moisture conditions considered in this problem. It must be pointed out, however, that the hydraulic resistance may become non-negligible for higher moisture levels.

Considering the results of the time-dependent analysis TD1 for both LM and CM cases, only slight differences are noticed between the three studied sections of the wall. Therefore, a macro-modeling strategy with equivalent masonry properties could be used as well to simulate the observed temperature and moisture content evolution. Notwithstanding the loss of detail, a simplified 1D model could be considered as well with a minor impact on the overall accuracy.

3.2.3. Time-Dependent Analysis with Variable External Boundary Conditions (TD2)

For the second group of time-dependent analyses, labeled TD2, the steady-state equilibrium (resulting from the SS analysis or the final stage of TD1) was taken as the initial condition of the wall. Moreover, the sinusoidal expressions for variable temperature and relative humidity described in Equations (20) and (21) were adopted so that the effect of time-dependent boundary conditions could be studied.

The results of the time-dependent analysis with variable boundary conditions, TD2, are shown in Figures 7 and 8, in terms of temperature and relative humidity variations, respectively. Note that the corresponding graphs show the imposed boundary conditions together with the response obtained for different points on the external and internal faces of the wall.

When considering the thermal response (see Figure 7), there are some discrepancies between the wall with lime mortar (LM) and the one with cement mortar (CM). In particular, the thermal properties of bricks and lime mortar are rather similar; thus, the obtained trends show comparable temperature values for the selected points on each side of the wall. Conversely, for the CM case, the results show different temperatures for the points located on mortar joints and brick surfaces. Moreover, the thermal excursion on the external side of the wall is similar in both cases. However, the temperature variation range for the CM case is slightly greater on the internal face. This can be explained by the higher conductivity of cement mortar. It is noted that the temperature on the outer surface shows a phase shift with respect to the external input. There is an additional shift between the external and the internal faces of the wall. In particular, the maximum and minimum temperature values are detected on the internal surface around 9–10 h later with respect to the peak values on the outer surface. The external/internal delay is shorter for the CM case, which can be related to the higher thermal conductivity of the cement mortar mentioned above.

Concerning the moisture response (see Figure 8), there are considerable differences between the two studied cases. In particular, the relative humidity values obtained for the LM case show only small disparities between the external points on mortar joints and brick surfaces. On the contrary, for the CM case, the results show significant differences between the relative humidity values obtained for the different points depending on their location. Furthermore, the relative humidity variation on the external side of the wall is greater for the cement mortar joints. In this context, the slower moisture response of the cement mortar (lower liquid diffusivity and water vapor permeability) can explain the greater and more shifted relative humidity excursion obtained for the mortar joints on the exterior surface. On the internal face, the CM case also shows a wider relative humidity

range. It must be noted that for any of the cases, the moisture response obtained for the internal face is directly related to the temperature variation, which affects the relative humidity through the saturation vapor pressure, such as $\varphi = p_v / p_{v,sat}(T)$. There is a significant delay between the external boundary condition and the moisture evolution on the external surface. It can be observed that the shift between the imposed conditions and the response of the external face of the wall is greater for moisture than for temperature. This was expected since mass transport is a slower process. Finally, there is an additional shift between the external and the internal faces of the wall. The external/internal shift is shorter for the CM case due to the shorter temperature delay mentioned before.

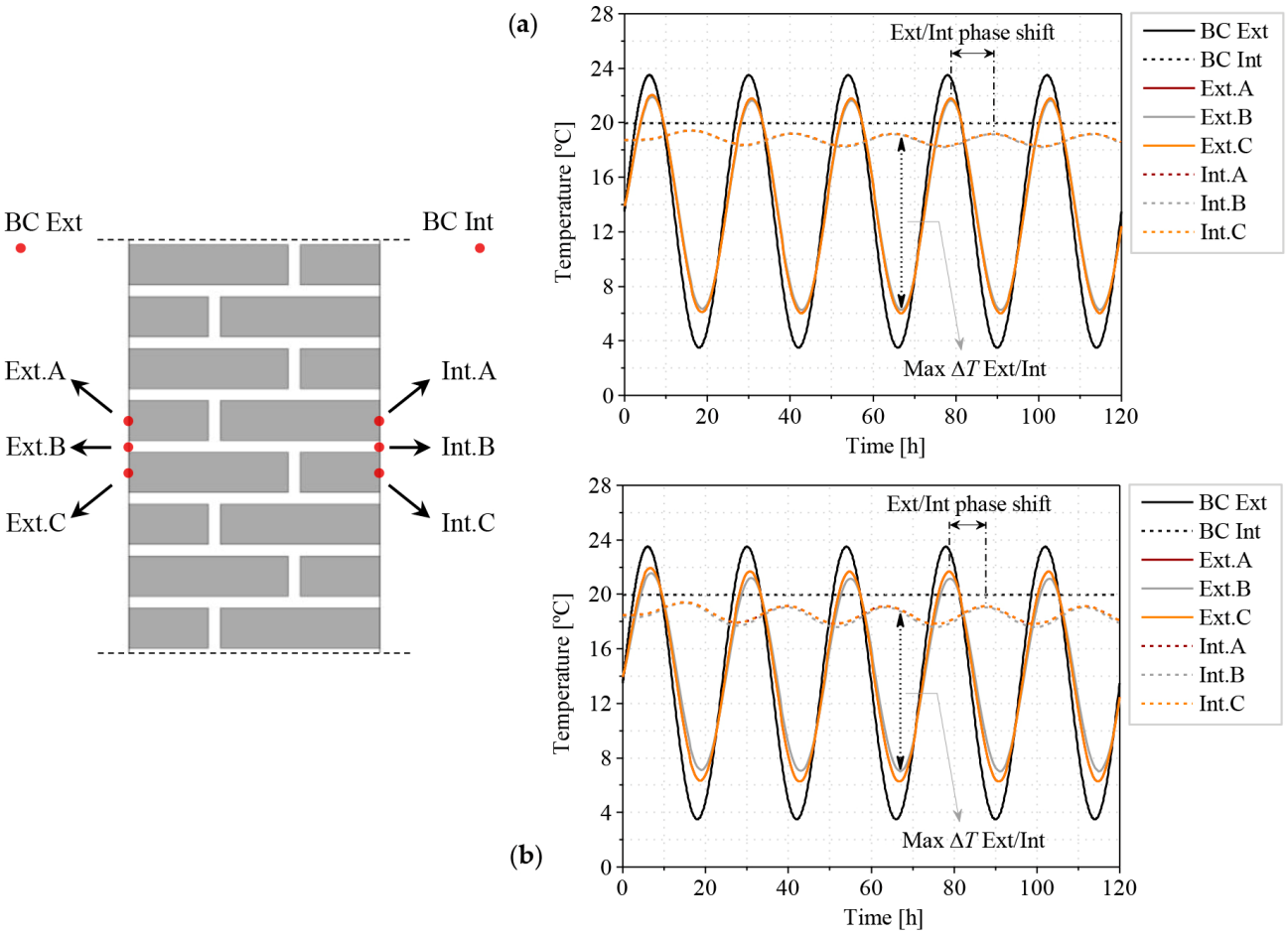

Figure 7. Time-dependent analysis with variable external boundary conditions (TD2). Temperature evolution for different points of the studied three-wythe brick masonry wall: (**a**) joints with natural hydraulic lime mortar (LM); (**b**) joints with cement mortar (CM).

Additionally, a parametric study was performed for the time-dependent analysis TD2 in order to evaluate the role of the brick–mortar interface on the moisture response. Consequently, the same analysis was performed using higher and lower values of the hydraulic resistance. Again, the results obtained with the new R_{IF} values did not show significant differences. Therefore, it was concluded that the impact of the hydraulic resistance is not significant for the boundary conditions considered in this problem. Nonetheless, it must be recalled that the influence of the interface may become non-negligible for higher moisture levels.

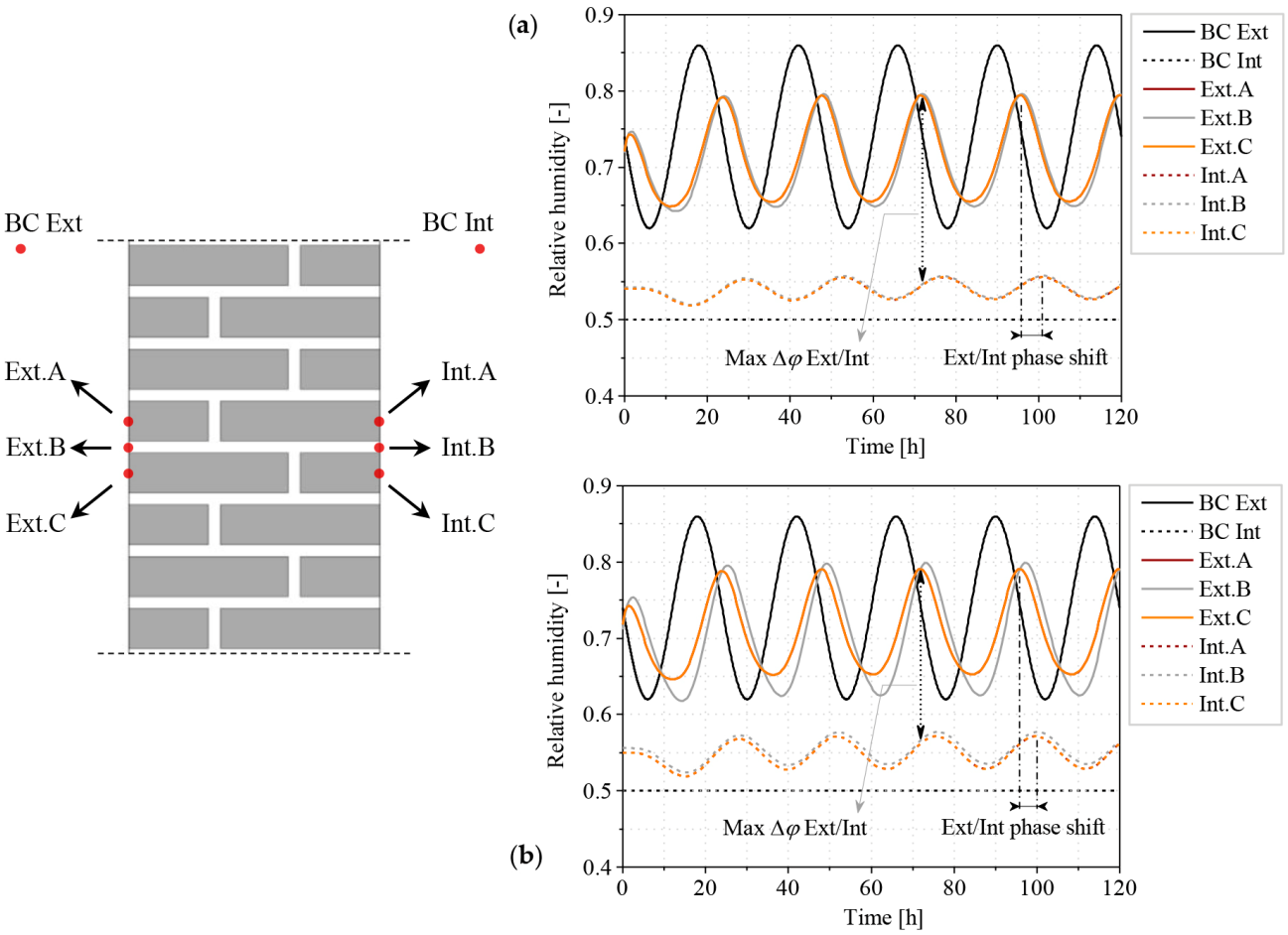

Figure 8. Time-dependent analysis with variable external boundary conditions (TD2). Evolution of the relative humidity for different points of the studied three-wythe brick masonry wall: (**a**) joints with natural hydraulic lime mortar (LM); (**b**) joints with cement mortar (CM).

Independently of the studied case, the response of the wall stabilizes (dynamic equilibrium) after a couple of cycles. It is noted that external/internal phase delay entails temperature and relative humidity gradients higher than the ones expected if the shift was not considered, and maximum and minimum values were occurring simultaneously at one and the other sides of the wall. In particular, the maximum thermal gradient obtained for the average temperatures between the two faces is $\Delta T = 13.0$ °C for the LM case and $\Delta T = 12.4$ °C for the CM case. In turn, the maximum moisture gradient obtained for the average relative humidity values between the two faces is $\Delta\varphi = 0.18$ for the LMJ case and $\Delta\varphi = 0.17$ for the CM case. Considering these aspects, a time-dependent analysis with variable boundary conditions may produce more severe scenarios and is, therefore, recommended for a better approximation of real environmental actions.

Considering the results described in the previous paragraphs, it is evident that the hygro-thermal behavior of brick masonry walls depends, to a great extent, on the type of mortar. When considering the wall with natural hydraulic lime mortar (LM), the temperature and relative humidity trends showed comparable values for the groups of studied points, independent of their location on brick or mortar joints. Therefore, this type of hygro-thermal problem could be simulated for the LM case by means of a macro-modeling approach with an equivalent masonry material or a simplified 1D model with hardly any loss of information. Conversely, the wall with cement mortar (CM) showed some differences in temperature and relative humidity depending on the material where

the studied point was located. Thus, for the CM case, the macro-modeling approach or the reduction to a 1D problem would entail a certain loss of detail and accuracy.

4. Hygro-Thermo-Mechanical Model

This section presents the numerical model employed for hygro-thermo-mechanical analysis. The main hypotheses and simplifications previously explained for the hygro-thermal models (see Section 2) are valid here as well. With respect to the structural mechanics field, a series of new assumptions must be introduced. In general, the environmental loads induced by normal exposure conditions are not expected to cause damage (at least not in the short term). Thus, the materials are likely to behave within the linear elastic range and material non-linearity is disregarded. Moreover, materials and structural elements are considered to be in an undamaged initial state. Finally, infinitesimal strains and small deformations and rotations are assumed.

4.1. Coupling between Heat, Moisture, and Mechanical Fields

The mechanical problem is linked to the thermal and moisture fields through the extended Duhamel–Neumann equation or total strain additive decomposition [65]; the total strain can be divided into different components: namely, mechanical-, thermal-, and moisture-induced strains. This is based on the assumption of infinitesimal strains and small deformations and rotations, which is generally applicable to masonry structures [24]:

$$\varepsilon = \varepsilon_{elastic} + \varepsilon_{plastic} + \varepsilon_{thermal} + \varepsilon_{swelling} \tag{22}$$

The mechanical strains $\varepsilon_{elastic}$ and $\varepsilon_{plastic}$ account for the effects caused by forces and moments, either in the elastic or inelastic ranges. On the other hand, the thermal and hygric strains are related to deformations caused by temperature and moisture variations, respectively.

The temperature-induced strain for an isotropic material is defined as:

$$\varepsilon_{thermal} = \alpha_T \Delta T = \alpha_T \left(T - T_{ref} \right) \tag{23}$$

where α_T [1/K] is the coefficient of thermal expansion of the material, and T_{ref} [K] is the reference temperature at which the thermally induced strain is zero.

An analogous relation may be written for the moisture-induced strain:

$$\varepsilon_{swelling} = \alpha_h \Delta w_g = \alpha_h \left(w_g - w_{g,ref} \right) \tag{24}$$

where α_h [–] is the moisture swelling coefficient of the material, w_g [kg/kg] is the gravimetric moisture content, and $w_{g,ref}$ [kg/kg] is the reference moisture content for which the moisture-induced strain is zero. Note that the moisture content may also appear as mass of absorbed water per volume of dry material, w [kg/m^3]. In that case, if α_h is initially given in terms of gravimetric moisture content (dimensionless), it must be divided by the density of the material, ρ_{bulk} [kg/m^3], to maintain the consistency of the units. Since the moisture content is dependent on the relative humidity by means of the moisture storage function, the moisture-induced strain is also a non-linear function of the relative humidity.

It is noted that the hygro-mechanical and thermo-mechanical coupling processes defined in this way involve a two-step procedure. First, the temperature and moisture profiles are obtained by means of the hygro-thermal analysis. Subsequently, the temperature and moisture results are used as input for the mechanical problem. Consequently, the proposed model consists of a one-way or unidirectional type of coupling, that is, heat and moisture fields have an impact on each other, and the hygro-thermal results are linked to the mechanical response, but the effects of the structural response on the temperature and moisture fields are not considered. It must be mentioned that the development of stresses and strains within a porous material may affect the hygric and thermal responses. For instance, Carmeliet et al. [66] studied the so-called mechano-sorptive behavior of porous

materials and concluded that the amount of moisture adsorbed by the material reduces as the specimens are subjected to higher compressive stresses. Additionally, these authors observed that the stress effect on the sorption behavior is more pronounced for higher relative humidity values. However, these mechanically induced effects are expected to be of minor importance for the stress limits considered in this work [23]. Thus, a schematic diagram of the proposed HTM model is provided in Figure 9.

A direct influence of thermal variations on the mechanical properties of masonry materials can be considered negligible for the temperature range of interest in this study. On the contrary, the mechanical performance of porous materials is generally affected by moisture, which may lead to a reduction of the mechanical properties [16]. Nonetheless, considering the lack of specific research dedicated to the moisture-dependent mechanical behavior of masonry materials, these aspects are neglected in the present study and further works on this topic are needed.

Under the assumption of linear elasticity and the described one-way coupled problem, the temperature- and moisture-induced strains are directly proportional to the results of the hygro-thermal problem by means of the thermal and hygric expansion coefficients.

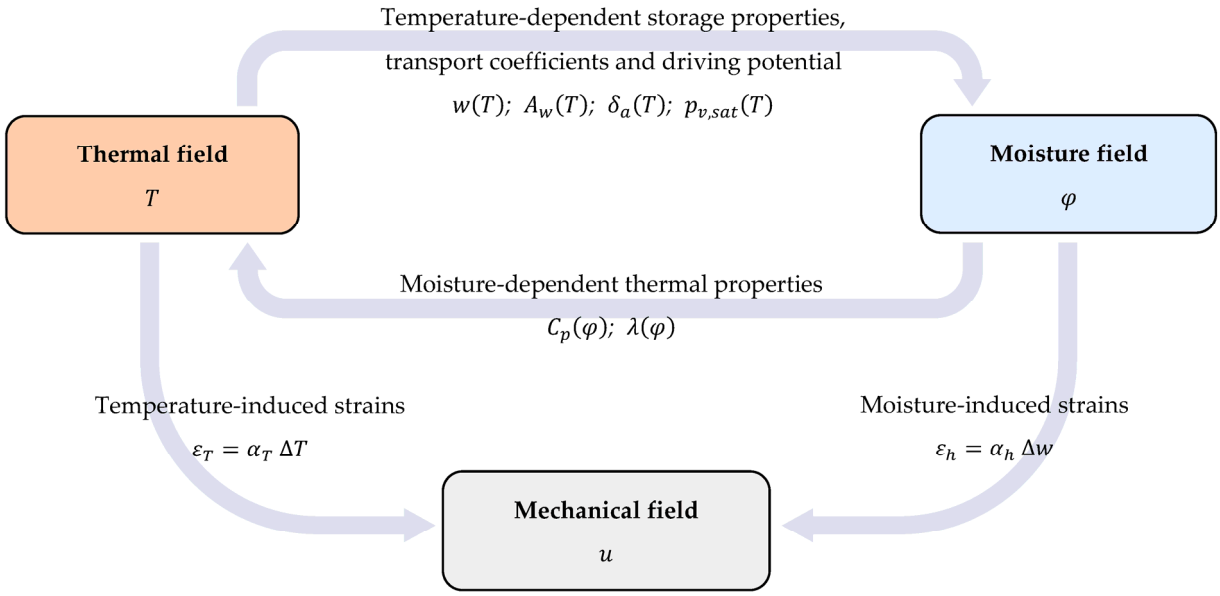

Figure 9. Schematic diagram of the proposed one-way coupled hygro-thermo-mechanical model.

4.2. Initial and Boundary Conditions

The equilibrium state of a porous building material is intimately related to the surrounding environmental conditions. Specifically, temperature and moisture content increments cause material dilation, whereas shrinkage takes place when temperature and relative humidity decrease. Moreover, these material responses give rise to the appearance and evolution of internal stresses. It is worth noting that the stresses induced by thermal or hygric volumetric variations are necessarily associated with a deformation constraint. In other words, if deformations are not restrained, the material will experience a free dimensional change and internal stresses will not appear. Nonetheless, constraints always exist in real applications, usually linked to the external boundary conditions or the presence of interfaces. Therefore, internal stresses caused by temperature and moisture content variations are expected. In this context, the initial conditions of the system are usually assumed as the initial equilibrium state. Since they are associated with no internal deformations, the initial conditions are commonly known as free-strain or zero-strain conditions.

5. Hygro-Thermo-Mechanical Simulations and Discussion

This section demonstrates the application of the hygro-thermo-mechanical (HTM) model using the previously introduced brick masonry wall as a case study. First, the description of the model is recalled, and the new parameters and boundary conditions needed for the mechanical component are defined. Then, the results of the HTM analyses are presented and discussed.

5.1. Description of the Numerical Model and Boundary Conditions

The same three-wythe brick masonry wall presented for the hygro-thermal simulations was used for the HTM analyses (see description of the model in Section 3.1). Similarly, the physical, thermal, and hygric material properties presented in Table 1 were employed for the model definition. The newly added properties needed for the mechanical field are introduced in Table 3. The numerical simulations were performed with a 2D plane strain finite element model using the software COMSOL Multiphysics [59].

Two different scenarios were studied: namely, a gravitational load case and a combined hygro-thermo-mechanical case. For the gravitational case, body forces were considered, including a uniformly distributed load, $L = 12.5$ kN/m, applied on top of the wall to simulate the weight of a simply supported roof. The HTM scenario was built upon the gravitational case so that the body forces were included. Moreover, for the HTM case, the temperature and moisture conditions defined previously for the time-dependent hygro-thermal analysis TD2 (see Section 3.1) were imposed on the wall. It is recalled that the TD2 analysis considers an initial step for the wall to reach the steady-state equilibrium with the environment. In other words, the wall is already in a deformed configuration (initial conditions to steady-state equilibrium) before the application of the variable boundary conditions.

Table 3. Summary of mechanical, thermo-mechanical, and hygro-mechanical properties used for the hygro-thermo-mechanical simulations.

Material	Property	Symbol	Value/Expression	Units	Source
Brick	Young's modulus	E	5580	MPa	Ghiassi et al. [67]
	Poisson's ratio	ν	0.20	–	
	Compressive strength	f_c	19.80	MPa	
	Tensile strength	f_t	2.00	MPa	
	Coefficient of thermal expansion	α_T	2.56×10^{-6}	1/°C	Ramirez et al. [18]
	Coefficient of hygric expansion	α_h	$1.40 \times 10^{-4}/{w_g}^{0.72}$	–	
Lime mortar (LM)	Young's modulus	E	3330	MPa	Penas et al. [68]
	Poisson's ratio	ν	0.20	–	
	Compressive strength	f_c	1.10	MPa	
	Tensile strength	f_b	0.40	MPa	
	Coefficient of thermal expansion	α_T	3.04×10^{-6}	1/°C	Ramirez et al. [18]
	Coefficient of hygric expansion	α_h	$3.00 \times 10^{-4}/{w_g}^{0.62}$	–	
Cement mortar (CM)	Young's modulus	E	2370	MPa	D'Altri et al. [35]
	Poisson's ratio	ν	0.20	–	
	Compressive strength	f_c	8.20	MPa	
	Tensile strength	f_t	1.50	MPa	
	Coefficient of thermal expansion	α_T	7.38×10^{-6}	1/°C	Ramirez et al. [18]
	Coefficient of hygric expansion	α_h	$1.32 \times 10^{-4}/{w_g}^{0.78}$	–	

Regarding the mechanical boundary conditions, the bottom of the wall is assumed to be fixed: that is, all degrees of freedom are constrained. Conversely, the uppermost edge is not restrained, and all degrees of freedom remain free. The wall is assumed to be in a non-deformed configuration before the application of the gravitational and environmental loads. Moreover, the initial temperature and relative humidity are $\vartheta_0 = 13.5$ °C and $\varphi_0 = 0.74$, respectively. For these conditions, the temperature- and moisture-induced strains are zero.

Assuming the applicability of Saint Venant's principle, the following discussion on the distribution of stresses focuses on a section of the mid-portion of the wall (height around 1.20 m). In other words, the area selected for the analysis of stresses is reasonably distant from any applied load or boundary condition that could directly influence the local stress/strain distribution.

5.2. Hygro-Thermo-Mechanical Behavior of a Brick Masonry Wall

The results of the HTM model presented in the previous section are examined in the following paragraphs. In particular, the behavior of the wall is studied in terms of minimum and maximum principal stresses, σ_3 and σ_1, according to the type of material and case scenario. The general sign convention is followed: thus, negative stresses indicate compression, and positive stresses denote tension. For the HTM analyses, the moment with maximum induced deformation (maximum horizontal displacement of the top of the wall) was chosen for the study. The selected deformed state is shown in Figures 10 and 11 for the LM and the CM cases, respectively, together with the history of displacements for the top of the wall and the imposed boundary conditions. Here, u and v are the displacements in the X and Y directions, respectively. It is recalled that the stress discussion is focused solely on a selected mid-height section of the wall.

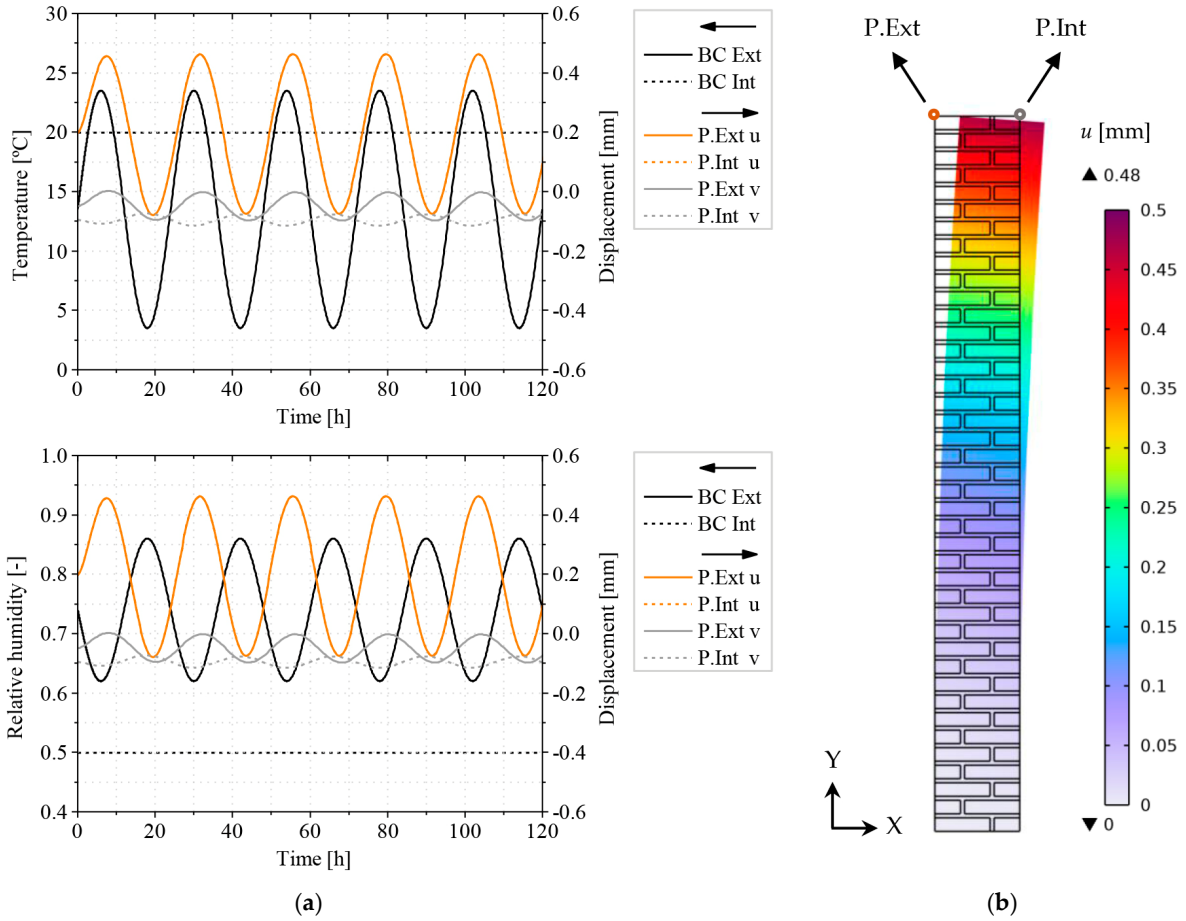

Figure 10. Hygro-thermo-mechanical analysis of the three-wythe brick masonry wall with natural hydraulic lime mortar: (**a**) imposed boundary conditions and displacement history measured at the top of the wall; (**b**) deformed shape selected for the study (maximum horizontal displacement).

When considering the displacement history for the LM case (see Figure 10), it is possible to observe the initial deformed configuration of the wall before the application of the variable external boundary conditions. In particular, the wall presents a horizontal displacement to-

wards the interior caused by moisture shrinkage of the internal face ($\varphi_{int} = 0.50 < \varphi_0 = 0.74$), which prevails over thermal dilation ($\vartheta_{int} = 20\ ^\circ\text{C} > \vartheta_0 = 13.5\ ^\circ\text{C}$). This horizontal displacement is approximately equal on the exterior and interior sides of the wall. On the other hand, the vertical displacement is rather small and remains always below 0.1 mm during the duration of the analysis. This vertical displacement is different on the exterior and interior sides of the wall due to rotation of the section. When the variable boundary conditions are implemented, the wall oscillates following the sinusoidal trend of the external temperature and relative humidity. In fact, the maximum horizontal displacement occurs with some delay after the external temperature peak (overall thermal expansion with greater dilation of the exterior face, i.e., $\vartheta_{ext} > \vartheta_{int} > \vartheta_0$) and after the minimum value of the external relative humidity (general shrinkage of the wall still more prominent on the internal face, i.e., $\varphi_{int} < \varphi_{ext} < \varphi_0$).

The displacements obtained for the wall with cement mortar (see Figure 11) follow the same trends described above for the LM case. However, the CM case shows larger deformations. This was expected considering the higher thermal expansion and hygric expansion coefficients of cement with respect to the lime mortar.

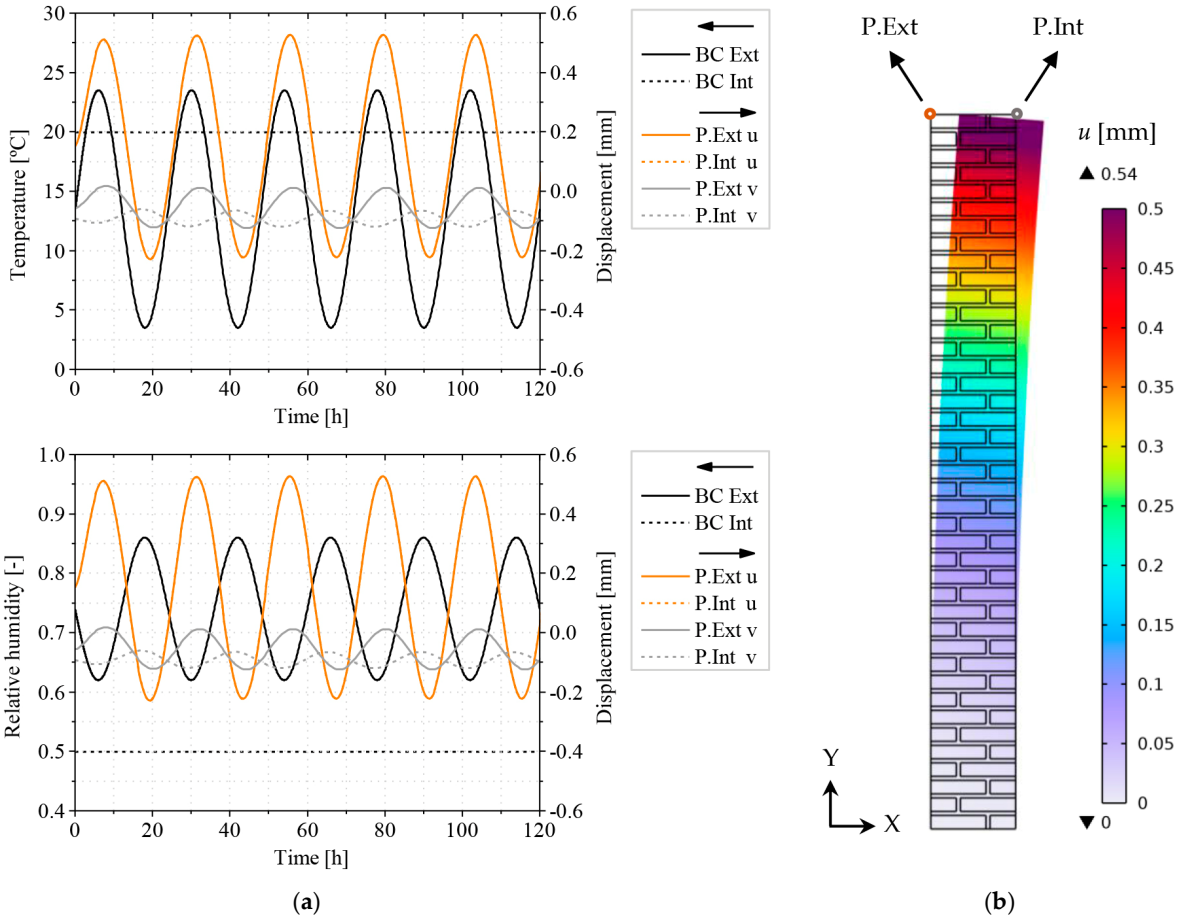

Figure 11. Hygro-thermo-mechanical analysis of the three-wythe brick masonry wall with cement mortar: (**a**) imposed boundary conditions and displacement history measured at the top of the wall; (**b**) deformed shape selected for the study (maximum horizontal displacement).

The stress state obtained for the LM case under the self-weight condition (body force plus roof weight) is shown in Figure 12. As expected, the distribution of minimum principal stresses (see Figure 12a,b) reveals a uniform level of compression in bricks and bed mortar joints, around −0.09 MPa for the selected area (note that compression increases with wall depth). Conversely, a 2D effect can be seen in the vertical head joints, which experience a lower compression level, around −0.06 MPa. A more detailed analysis of the stress

distribution in bricks brings to light two aspects: (a) the compression stress is slightly lower, around −0.08 MPa, in the mid-section of the header course bricks, that is, the portion of the brick aligned with the vertical head joints; (b) higher compression values, ca. −0.10 MPa, are found on the vertical edges of the bricks adjacent to mortar head joints. Therefore, the brick–mortar interaction is associated with 2D phenomena that affect the distribution of stresses within the masonry wall.

The maximum principal stresses obtained for the gravitational case reveal expected trends as well (see Figure 12c,d). On one hand, the positive component of the principal stress for bricks is practically zero, whereas it presents low positive values for the vertical head joints, around 5.0×10^{-3} MPa. Even though the obtained values are not significant, this observation is consistent with the fact that head joints typically act as tension planes within the wall geometry. On the other hand, the results for the horizontal joints show small negative values for σ_1, around -8.0×10^{-3} MPa, which indicates that the bed mortar joints experience biaxial compression. Moreover, the maximum principal stress in the bed joints drops to zero in the regions near the external and internal faces of the wall.

The distribution of stresses for the CM wall under gravitational loads is shown in Figure 13. It is noted that the obtained results are analogous to the ones of the LM case. In this sense, the distribution of minimum principal stresses for bricks and mortar bed joints (see Figure 13a,b) presents the same average compression, i.e., −0.09 MPa. Likewise, the areas of the bricks aligned with vertical joints show lower stresses, ca. −0.08 MPa. Some differences between the two cases can be pointed out as well. For instance, the compression values on the vertical edges of the bricks adjacent to mortar head joints are slightly higher, around −0.11 MPa. Moreover, the vertical joints show less compressive stresses, ca. −0.05 MPa.

The distribution of maximum principal stresses for the wall with cement mortar (see Figure 13c,d) shows some differences with respect to the LM case as well. The positive component of the principal stress for bricks is still negligible for most of the wall, but higher values appear close to the brick corners, between 5.0×10^{-3} and 6.0×10^{-3} MPa. Furthermore, higher σ_1 values can be found in the vertical head joints, ca. 7.0×10^{-3} MPa. Although the obtained tensile stresses are low, they may contribute to crack propagation when cracks are already present. On the other hand, the horizontal joints show lower negative values, around −0.01 MPa; thus, they undergo a biaxial compression state. Finally, the maximum principal stress in bed joints falls to zero in the regions near the faces of the wall.

In conclusion, for the two studied models, the outcomes of the gravitational case reveal a complex 2D stress distribution derived from the multi-layered nature of the material. Moreover, the stress distribution results for the LM and CM walls are analogous, although slightly higher stress states are obtained for the wall with cement mortar.

Regarding the HTM analysis, the stress distribution results obtained for the LM case are shown in Figure 14. It is recalled that the instant with maximum horizontal displacement is selected for the analysis (see Figure 10). At that moment, the imposed boundary conditions lead to shrinkage of the internal face of the wall. It is noted that the corresponding deformed configuration is intimately linked to the stress distribution. As expected, the distribution of stresses is not uniform across the wall thickness. Considering the minimum principal stresses (see Figure 14a,b), lower compression values are found in the middle portion of the wall, around −0.07 MPa. Conversely, higher stresses appear near the external and internal faces, ca. −0.12 MPa. The compressive stresses in bed mortar joints follow a similar trend with values around −0.13 MPa near the wall boundaries. On the other hand, the results of σ_3 in head mortar joints show lower compression levels, with values around −0.05 MPa and −0.04 MPa for the vertical joints located closer to the external and internal surfaces, respectively. Finally, the bricks show the same trends observed for the gravitational case: namely, lower compressive stresses in the areas aligned with the vertical joints and higher concentration of stresses near the vertical edges adjacent to mortar head joints.

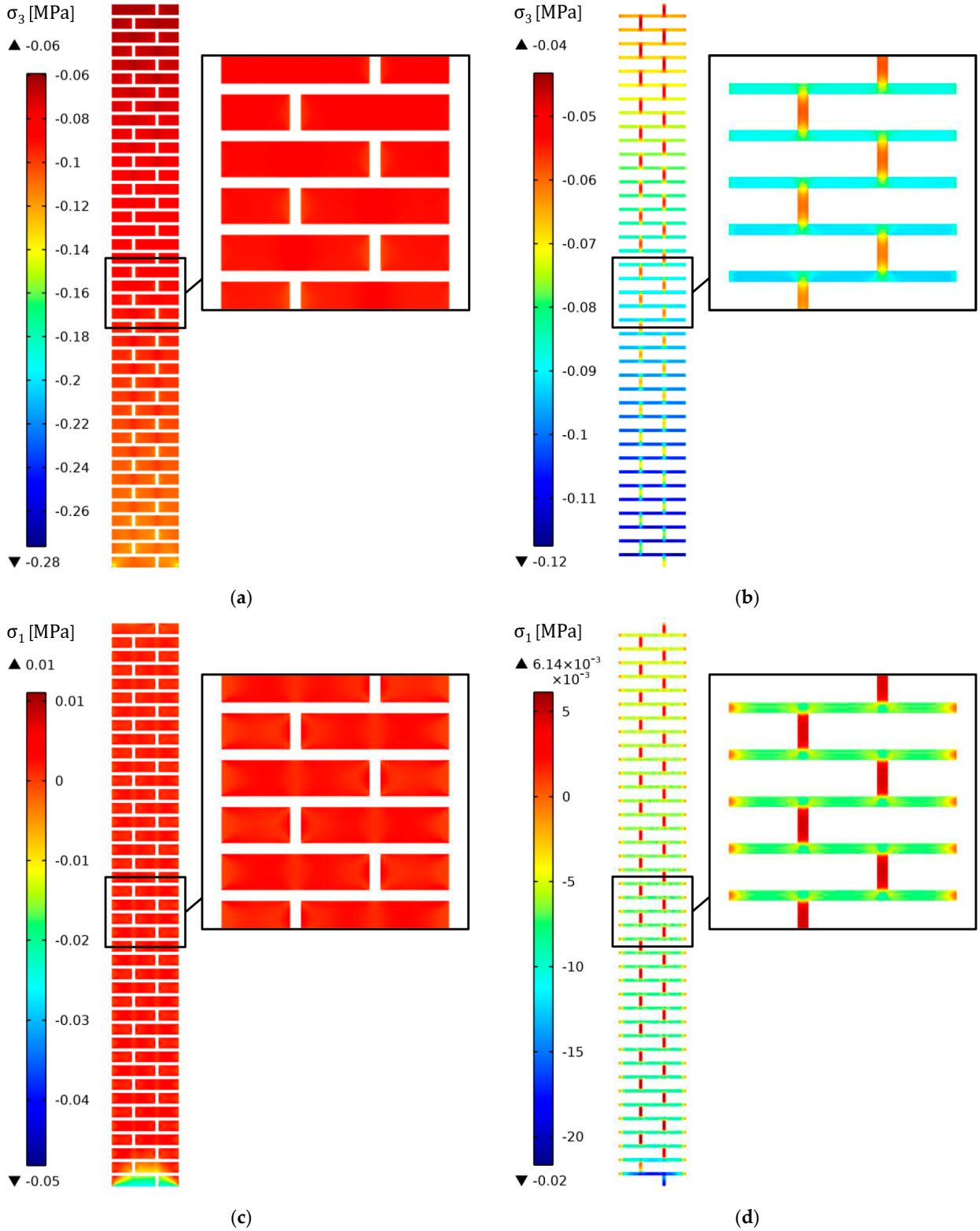

Figure 12. Hygro-thermo-mechanical analysis of the three-wythe brick masonry wall with natural hydraulic lime mortar. Principal stress distribution obtained for the gravitational loads alone: minimum principal stress, σ_3 [MPa], in (**a**) bricks and (**b**) mortar joints; maximum principal stress, σ_1 [MPa], in (**c**) bricks and (**d**) mortar joints.

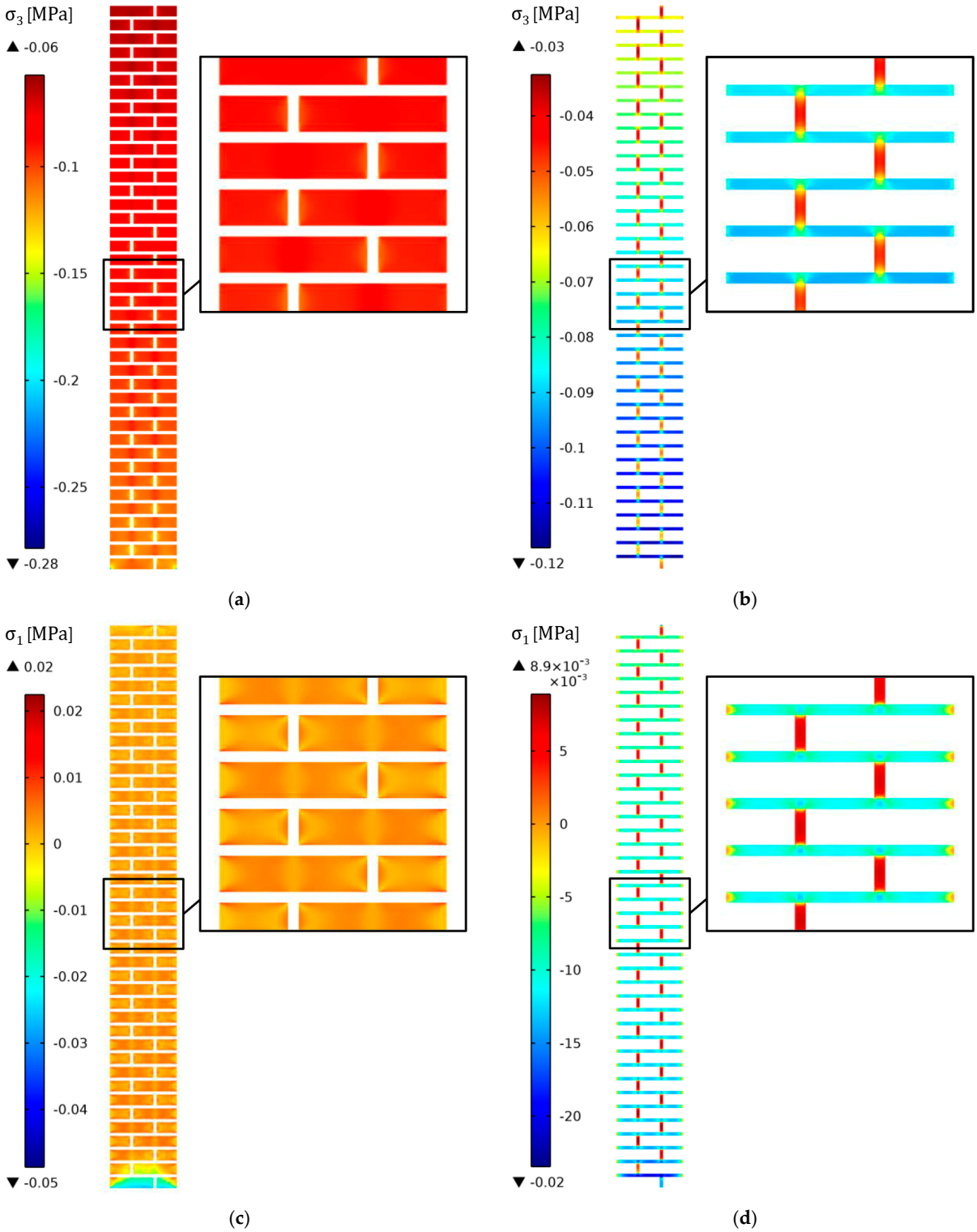

Figure 13. Hygro-thermo-mechanical analysis of the three-wythe brick masonry wall with cement mortar. Principal stress distribution obtained for the gravitational loads alone: minimum principal stress, σ_3 [MPa], in (**a**) bricks and (**b**) mortar joints; maximum principal stress, σ_1 [MPa], in (**c**) bricks and (**d**) mortar joints.

The distribution of maximum principal stresses for the LM case (see Figure 14c,d) presents a relatively uniform gradient across the wall thickness with negligible negative values near the external surface and higher tensile stresses close to the internal side of the wall. In fact, the

highest positive values are detected in the outermost layer of the elements facing the interior: namely, 0.06 MPa for bricks and 0.05 MPa for bed mortar joints. The maximum principal stresses for vertical head joints depend on the location: namely, 0.01 MPa and 0.04 MPa for the joints closer to the exterior and the interior faces, respectively.

The HTM results for the CM wall are depicted in Figure 15. As happened with the gravitational loads, the overall stress distribution is analogous to the one obtained for the LM case. This was expected since the deformed shape is similar for both cases. Nonetheless, several differences can be pointed out. The minimum principal stresses for bricks (see Figure 15a) present a non-uniform distribution with lower values in the middle section, ca. −0.07 MPa, and higher stress concentration near the external and internal faces: namely, −0.14 MPa and −0.12 MPa, respectively. A similar distribution is found in the bed joints (see Figure 15b), with greater compressive stresses near the outer surface, ca. −0.15 MPa. On the other hand, the head joints show values around −0.07 MPa and −0.04 MPa for the vertical joints located closer to the external and internal surfaces, respectively. As for the previous cases, the bricks present lower compressive stresses in the areas aligned with the vertical joints and a higher concentration of stresses near the vertical edges adjacent to the head joints.

The maximum principal stresses obtained for the CM case (see Figure 15c,d) present a relatively uniform gradient across the thickness of the wall. The σ_1 results for bricks (see Figure 15c) show generalized tensile stresses with increasing values for areas closer to the internal surface, around 0.06 MPa. Furthermore, significant concentrations of tensile stresses (values up to 0.12 MPa) appear on the brick corners adjacent to horizontal joints near the external face. Additionally, the σ_1 results for bed joints (see Figure 15d) show a rather uniform stress gradient through the wall thickness, with negative values near the external surface, ca. −0.07 MPa, and a transition towards tensile values on the internal side, up to 0.02 MPa. It is noted that the maximum principal stress in the bed joints drops to negligible values in the regions near the external and internal faces of the wall. Finally, the maximum principal stresses for vertical joints are around 0.01 MPa, slightly higher on the head joints closer to the interior boundary.

In conclusion, for both models, the imposed hygro-thermal conditions induce deformations and lead to relevant changes in the stress state of the wall with respect to the gravitational case. For the specific boundary conditions considered in this study, the shrinkage of the internal face of the wall results in an uneven distribution of stresses across the wall thickness. In general, lower compression values appear in the middle portion, whereas higher compressive stresses are found in the elements near the wall surfaces. The vertical joints show a non-symmetrical stress distribution as well, with higher compression and higher tensile levels in the joints closer to the external and the internal faces, respectively. For the same hygro-thermal boundary conditions, the wall with cement mortar presents greater deformations (see Figure 11). Consequently, the HTM results for the CM case reveal higher stress levels in comparison with the wall built with LM. In particular, larger compression values are found on the external face, which can be explained by the higher coefficient of thermal expansion of cement mortar.

5.3. Influence of the Initial Conditions on the Hygro-Thermo-Mechanical Response

It is recalled that the thermal- and moisture-induced strains are dependent on the specific initial temperature and relative humidity values for which the free-strain or zero-strain condition is assumed. As a result, the initial conditions play a major role in the HTM analysis. For instance, the results presented in the previous section were calculated assuming that the wall had initial conditions equal to the average temperature and relative humidity of the exterior environment, i.e., 13.5 °C and 74% RH. However, if the initial conditions of the wall were assumed equal to the interior space, i.e., 20 °C and 50% RH, the obtained results would change drastically. Note that the steady-state hygro-thermal equilibrium reached by any of these two cases would be the same. However, the deformed configuration attained with the steady-state equilibrium does depend on the chosen hygro-thermal conditions used as a reference, see Equations (23) and (24). For the sake of clarity,

Figure 16 shows the maximum horizontal displacement obtained for the HTM analysis discussed in the previous section performed on the same LM and CM cases but assuming different initial conditions.

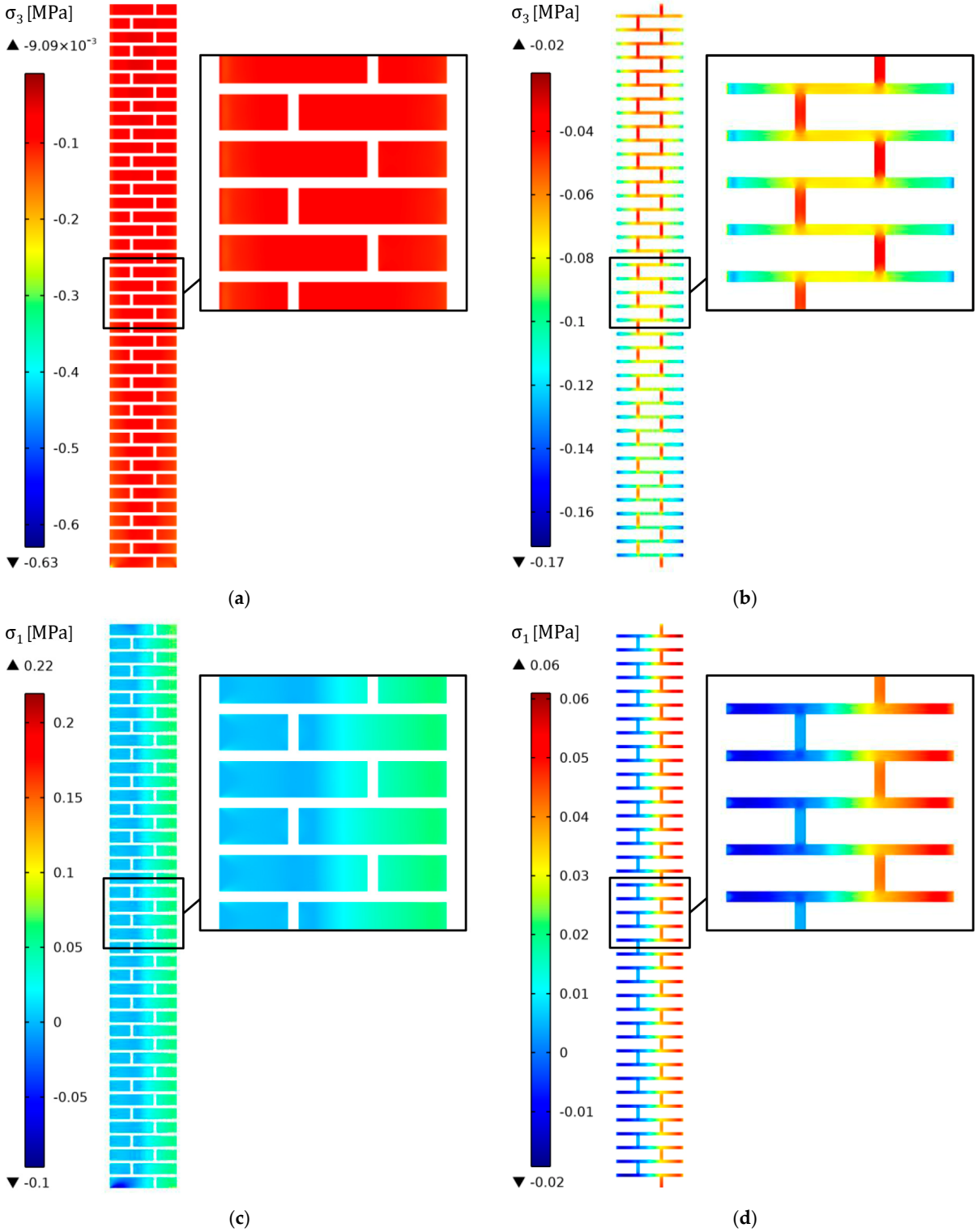

Figure 14. Hygro-thermo-mechanical analysis of the three-wythe brick masonry wall with natural hydraulic lime mortar. Principal stress distribution obtained for the hygro-thermo-mechanical case: minimum principal stress, σ_3 [MPa], in (**a**) bricks and (**b**) mortar joints; maximum principal stress, σ_1 [MPa], in (**c**) bricks and (**d**) mortar joints.

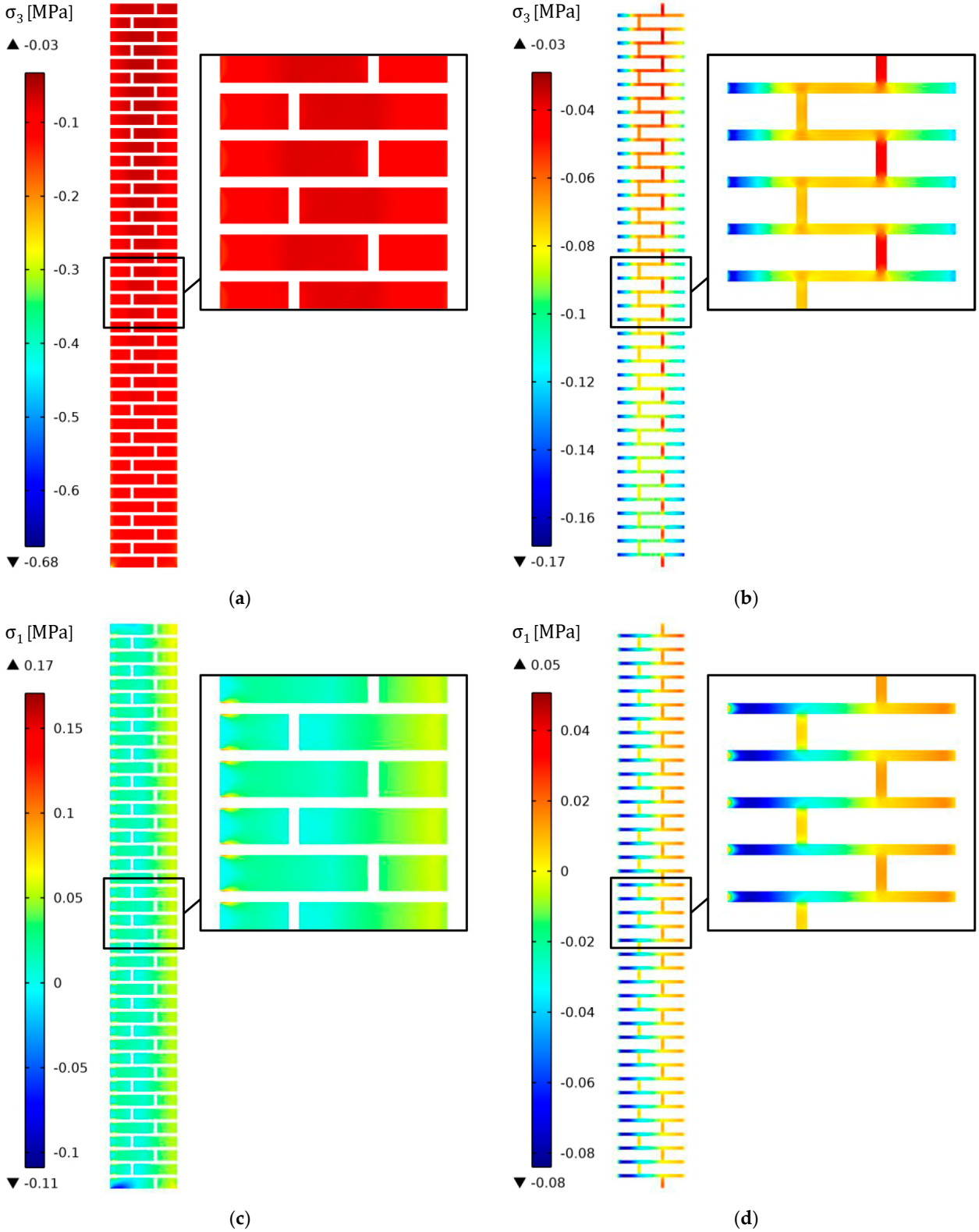

Figure 15. Hygro-thermo-mechanical analysis of the three-wythe brick masonry wall with cement mortar. Principal stress distribution obtained for the hygro-thermo-mechanical case: minimum principal stress, σ_3 [MPa], in (**a**) bricks and (**b**) mortar joints; maximum principal stress, σ_1 [MPa], in (**c**) bricks and (**d**) mortar joints.

It is worth recalling that the coefficient of thermal expansion, α_T, has been assumed constant. Therefore, the thermally induced strains are directly proportional to the imposed temperature gradient, ΔT. Consequently, assuming $\Delta T = T_{high} - T_{low}$, where $T_{high} > T_{low}$, the positive gradient leads to a positive strain and, thus, dilation or swelling. Conversely, the same gradient with a negative sign, i.e., $\Delta T = T_{low} - T_{high}$, would produce the same absolute value for the strain but, in this case, associated with shrinkage. As a result, the initial conditions defined for a thermo-mechanical analysis determine whether the material undergoes dilation or contraction, but the absolute value of the resulting strain would be the same.

On the contrary, it must be noted that the moisture-induced strains greatly depend on the initial conditions for which the zero-strain configuration is assumed. This behavior is due to the non-linear nature of the coefficient of hygric expansion, α_h. In order to illustrate this, the previously introduced brick wall with natural hydraulic lime mortar can be used as an example. Assuming $\varphi_{50} = 0.50$, the coefficient of hygric expansion for brick is $\alpha_h(\varphi_{50}) = 11.8 \times 10^{-6}$ m^3/kg. Moreover, for $\varphi_{74} = 0.74$, the corresponding coefficient for brick is $\alpha_h(\varphi_{74}) = 5.6 \times 10^{-6}$ m^3/kg. Lime mortar presents a similar trend: namely, $\alpha_h(\varphi_{50}) = 7.9 \times 10^{-6}$ m^3/kg and $\alpha_h(\varphi_{74}) = 4.2 \times 10^{-6}$ m^3/kg. Therefore, the coefficients of hygric expansion of both materials double for φ_{50} in comparison with φ_{74}. This implies that if the initial conditions are considered as the free-strain equilibrium, a drying wall ($\Delta\varphi = \varphi_{74} - \varphi_{50}$) will experience greater deformations than the same material becoming wet ($\Delta\varphi = \varphi_{50} - \varphi_{74}$). In conclusion, the initial conditions defined for a hygro-mechanical problem not only determine whether the material experiences swelling or shrinkage but also affect the extent of such deformation. Hence, a careful examination of the initial conditions must be considered for the analysis and interpretation of hygro-mechanical results.

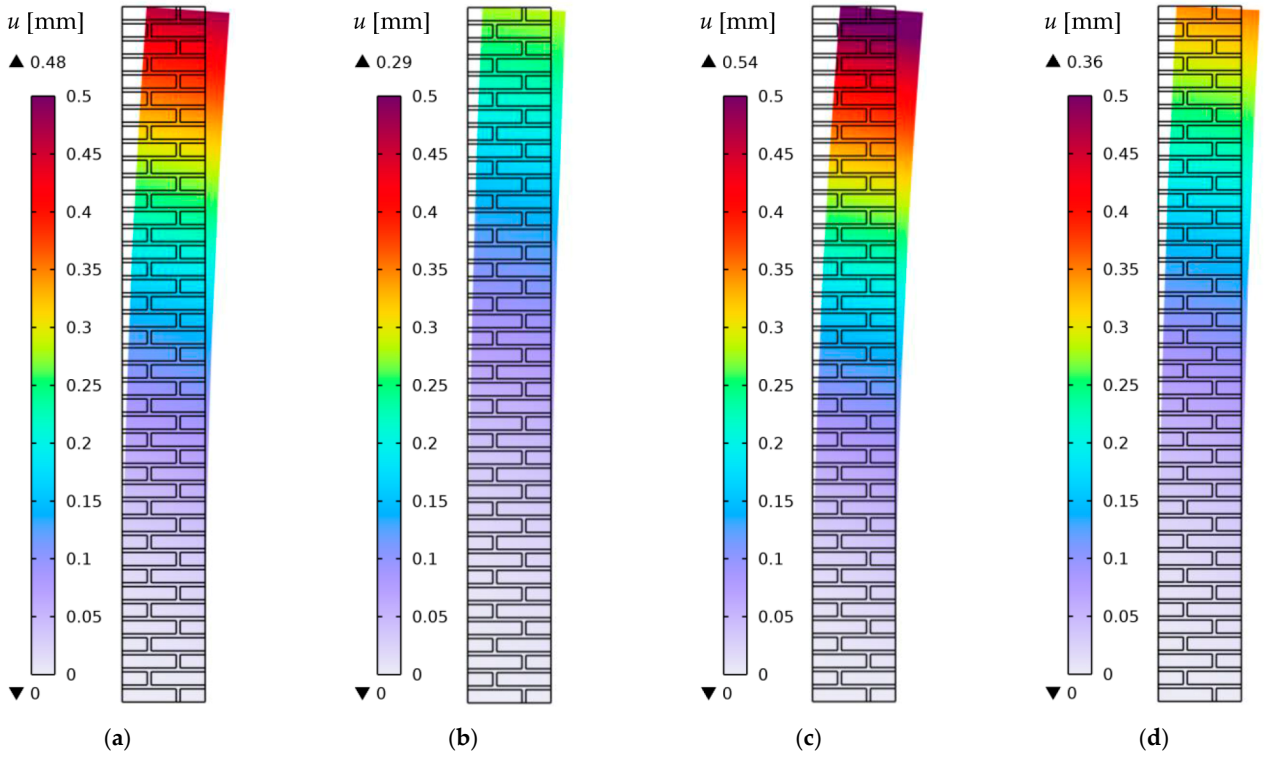

Figure 16. Hygro-thermo-mechanical analysis of the studied three-wythe brick masonry wall: maximum displacement obtained for the wall with natural hydraulic lime mortar assuming initial conditions equal to (**a**) external conditions and (**b**) internal conditions; maximum displacement for the wall with cement mortar assuming initial conditions equal to (**c**) external conditions and (**d**) internal conditions.

6. Conclusions

This paper presents a hygro-thermo-mechanical (HTM) model and its application to simulate how different hygro-thermal phenomena affect the structural behavior of masonry elements. First, the hygro-thermal model was presented together with the coupling assumptions needed to link the temperature and moisture fields. Subsequently, a finite element masonry wall was prepared and different hygro-thermal simulations were performed using COMSOL Multiphysics. In the second stage, the hygro-thermal model was extended to incorporate mechanical effects and a one-way coupled HTM model was presented. The capabilities of the HTM analysis were tested on the same masonry wall studied for the hygro-thermal analyses.

The presented work addresses the gap found in the literature regarding the impact of normal environmental actions on the structural response of masonry elements; namely, experimental studies are normally conducted under controlled, standard laboratory conditions, and numerical simulations usually neglect the influence of hygro-thermal loads by assuming ideal scenarios. Thus, the influence of temperature and moisture variations caused by actual environmental conditions are usually disregarded and so are the hygro-thermally induced stresses. Furthermore, examples of transient HTM analyses for variable environmental conditions are still lacking in the literature.

A 2D finite element model was prepared to simulate a three-wythe brick masonry wall under different hygro-thermal scenarios. Two types of mortars were considered: namely, natural hydraulic lime mortar (LM) and cement mortar (CM). The corresponding boundary conditions were defined based on the climate records of Guimarães (Portugal). Subsequently, steady-state (SS) analysis, time-dependent analysis with constant boundary conditions (TD1), and time-dependent analysis with variable boundary conditions (TD2) were performed. The results of these hygro-thermal studies were evaluated in terms of temperature and relative humidity distributions across the thickness of the wall as well as for different points on the external and internal surfaces. It was found that for the SS and TD1 analyses, there were only minor differences between the LM and the CM cases. Thus, for these scenarios, the wall can be simulated following a macro-modeling approach with equivalent masonry properties. Similarly, the system can be simplified into a 1D analysis without compromising the accuracy of results. The evolution of temperature and relative humidity profiles obtained by transient analyses show that heat transfer is significantly faster than moisture transport. In fact, thermal processes can be considered instantaneous in comparison with mass transfer. Considering the transient analysis TD2, the results showed differences in the hygro-thermal performance of the wall depending on the type of mortar. As expected, the LM case showed a more uniform response due to the similar behavior of bricks and lime mortar. On the contrary, the CM case presented localized behavior depending on the material. Thus, the LM case can be simplified to a 1D macro-modeling approach, but the same process applied to the CM wall may result in a loss of detail and accuracy. Finally, the interface hydraulic resistance at the brick–mortar interfaces did not play a role when considering the moisture conditions defined in this study.

The mechanical problem was coupled with the thermal and moisture fields through the total strain additive decomposition principle. According to this principle, the total strain can be divided into different components: namely, mechanical strains, temperature-induced strains, and moisture-induced strains. The thermal and hygric strains stem from the presence of a temperature gradient or a moisture gradient, respectively. Moreover, the induced strains are proportional to thermo-mechanical and hygro-mechanical parameters: namely, the coefficient of thermal expansion and the coefficient of hygric expansion. In the proposed HTM model, the link between the mechanical component and the hygro-thermal fields consists of a one-way coupled relationship. In other words, the hygro-thermal results affect the mechanical response, but mechanical stresses/strains do not influence heat and moisture transport. Additionally, temperature and moisture dependencies of the mechanical properties were not considered. The HTM model was completed with

the implementation of mechanical boundary conditions as well as the initial or free-strain conditions. A careful definition of initial and boundary conditions is of special importance for mechanical analyses since the appearance and distribution of stresses largely depend on these parameters. In particular, when considering the non-linear behavior of the coefficient of hygric expansion, the definition of the initial moisture conditions (and, therefore, the associated free-strain state) greatly affects the stress evolution.

The three-wythe brick masonry model defined for the hygro-thermal analysis was further used to study the internal distribution of stresses of the wall subjected to temperature and moisture gradients. In particular, the temperature and moisture results from the time-dependent analysis TD2 were used as input for the mechanical study. The instant of maximum displacement was chosen, and the corresponding stress distribution induced by the hygro-thermal loads was compared with the self-weight scenario. The analysis focused on a section of the mid-portion of the wall in order to avoid disturbances caused by the proximity of loads or boundary conditions. It was proven that temperature and moisture variations change the natural stress distribution of the wall subjected to gravitational loads alone. Moreover, the brick wall with cement mortar underwent higher stress levels in comparison with the wall with natural hydraulic lime mortar. This was caused by the higher thermal expansion and hygric expansion coefficients of cement in comparison with lime mortar. Although the induced tensile stresses were low, they may contribute to crack propagation of existing cracks. Similarly, the hygro-thermally induced deformations may add up to previous damage and magnify existing problems such as tilting in structures with moisture deterioration at the base or soil permanent deformation. Finally, it is noted that the hygro-thermo-mechanical behavior of the brick wall is a 2D phenomenon derived from the multi-layered nature of masonry.

The numerical approach presented in this paper can be used to evaluate the hygro-thermal performance of masonry walls as well as to complement the structural assessment when considering other static or dynamic loads. The methodology can be further extended to study the compatibility between masonry units and mortars. Taking into consideration the everyday nature and relevance of hygro-thermo-mechanical problems, the need for further investigation on this topic is evident. Similarly, experimental studies aimed at acquiring data for validation of the corresponding models are needed. Future works should extend the hygro-thermo-mechanical model to incorporate non-linear material behavior, with different constitutive laws for tension and compression and the capacity to reproduce creep. Likewise, improvements could be achieved by extending the simulations to 3D models, which are more suitable to reproduce complex hygro-thermal phenomena such as thermal bridges in envelope walls. Moreover, the study may be expanded to incorporate different heat and moisture regimes according to specific climatic zones. Finally, considering the cyclic nature of hygro-thermal phenomena, the study of material fatigue is strongly recommended.

Author Contributions: Conceptualization, R.R., B.G., P.P. and P.B.L.; methodology, R.R., B.G., P.P. and P.B.L.; software, R.R.; validation, R.R.; formal analysis, R.R.; investigation, R.R.; writing—original draft preparation, R.R.; writing—review and editing, B.G., P.P. and P.B.L.; visualization, R.R.; supervision, B.G., P.P. and P.B.L.; project administration, P.B.L.; funding acquisition, P.B.L. All authors have read and agreed to the published version of the manuscript.

Funding: This work was partly financed by FCT/MCTES through national funds (PIDDAC) under the R&D Unit Institute for Sustainability and Innovation in Structural Engineering (ISISE), under reference UIDB/04029/2020, and under the Associate Laboratory Advanced Production and Intelligent Systems ARISE under reference LA/P/0112/2020. The first author acknowledges the financial support provided by FCT—Foundation for Science and Technology, under grant agreement SFRH/BD/117114/2016. The APC was funded by MDPI's Invited Paper Program.

Institutional Review Board Statement: Not applicable.

Data Availability Statement: Not applicable.

Conflicts of Interest: The authors declare no conflict of interest.

References

1. Ghiassi, B.; Lourenço, P.B. (Eds.) *Long-Term Performance and Durability of Masonry Structures: Degradation Mechanisms, Health Monitoring and Service Life Design*, 1st ed.; Woodhead Publishing: Cambridge, UK, 2019; ISBN 9780081021101.
2. Brooks, J.J. Moisture Movement of Clay Brick Masonry. In *Concrete and Masonry Movements*; Elsevier: Oxford, UK, 2015; pp. 223–253.
3. Lourenço, P.B.; Milani, G.; Tralli, A.; Zucchini, A. Analysis of Masonry Structures: Review of and Recent Trends in Homogenization Techniques. *Can. J. Civ. Eng.* **2007**, *34*, 1443–1457. [CrossRef]
4. Angelillo, M.; Lourenço, P.B.; Milani, G. *Mechanics of Masonry Structures*; Angelillo, M., Ed.; CISM International Centre for Mechanical Sciences; Elsevier: Vienna, Austria, 2014; Volume 551, ISBN 978-3-7091-1773-6.
5. Lourenço, P.B. Computational Strategies for Masonry Structures: Multi-Scale Modeling, Dynamics, Engineering Applications and Other Challenges. In Proceedings of the Congress on Numerical Methods in Engineering CMN 2013, Bilbao, Spain, 25–28 July 2013; pp. 1–17.
6. Straube, J.F.; Burnett, E.F.P. Overview of Hygrothermal (HAM) Analysis Methods. In *Moisture Analysis and Condensation Control in Building Envelopes–ASTM Manual Series MNL 40*; Trechsel, H.R., Ed.; American Society for Testing and Materials: West Conshohocken, PA, USA, 2001; pp. 81–89.
7. Künzel, H.M.; Karagiozis, A.N.; Holm, A.H. A Hygrothermal Design Tool for Architects and Engineers (WUFI ORNL/IBD). In *Moisture Analysis and Condensation Control in Building Envelopes–ASTM Manual Series MNL 40*; Trechsel, H.R., Ed.; American Society for Testing and Materials: West Conshohocken, PA, USA, 2001; pp. 136–151.
8. Hens, H. Modeling the Heat, Air, and Moisture Response of Building Envelopes: What Material Properties Are Needed, How Trustful Are the Predictions? *J. ASTM Int.* **2007**, *4*, 1–11. [CrossRef]
9. Brocken, H.J.P. Moisture Transport in Brick Masonry: The Grey Area between Bricks. Ph.D. Thesis, Dept. Built Environment, Technische Universiteit Eindhoven, Eindhoven, The Netherlands, 1998.
10. Derluyn, H.; Janssen, H.; Carmeliet, J. Influence of the Nature of Interfaces on the Capillary Transport in Layered Materials. *Constr. Build. Mater.* **2011**, *25*, 3685–3693. [CrossRef]
11. Calle, K.; de Kock, T.; Cnudde, V.; van den Bossche, N. Liquid Moisture Transport in Combined Ceramic Brick and Natural Hydraulic Lime Mortar Samples: Does the Hygric Interface Resistance Dominate the Moisture Transport? *J. Build. Phys.* **2019**, *43*, 208–228. [CrossRef]
12. Zhou, X.; Desmarais, G.; Vontobel, P.; Carmeliet, J.; Derome, D. Masonry Brick–Cement Mortar Interface Resistance to Water Transport Determined with Neutron Radiography and Numerical Modeling. *J. Build. Phys.* **2020**, *44*, 251–271. [CrossRef]
13. Vereecken, E.; Roels, S. Hygric Performance of a Massive Masonry Wall: How Do the Mortar Joints Influence the Moisture Flux? *Constr. Build. Mater.* **2013**, *41*, 697–707. [CrossRef]
14. Jensen, N.F.; Bjarløv, S.P.; Rode, C.; Møller, E.B. Hygrothermal Assessment of Four Insulation Systems for Interior Retrofitting of Solid Masonry Walls through Calibrated Numerical Simulations. *Build. Environ.* **2020**, *180*, 107031. [CrossRef]
15. Soulios, V.; Jan de Place Hansen, E.; Peuhkuri, R. Hygrothermal Performance of Hydrophobized and Internally Insulated Masonry Walls–Simulating the Impact of Hydrophobization Based on Experimental Results. *Build. Environ.* **2021**, *187*, 107410. [CrossRef]
16. Castellazzi, G.; de Miranda, S.; Formica, G.; Molari, L.; Ubertini, F. Coupled Hygro-Mechanical Multiscale Analysis of Masonry Walls. *Eng. Struct.* **2015**, *84*, 266–278. [CrossRef]
17. Zhou, X.; Carmeliet, J.; Derome, D. Assessment of Moisture Risk of Wooden Beam Embedded in Internally Insulated Masonry Walls with 2D and 3D Models. *Build. Environ.* **2021**, *193*, 107460. [CrossRef]
18. Ramirez, R.; Ghiassi, B.; Pineda, P.; Lourenço, P.B. Experimental Characterization of Moisture Transport in Brick Masonry with Natural Hydraulic Lime Mortar. *Build. Environ.* **2021**, *205*, 108256. [CrossRef]
19. Conceição, J.; Faria, R.; Azenha, M. Thermo–Mechanical Analysis of an Arch Dam Monolith During Construction. In Proceedings of the Congress on Numerical Methods in Engineering CMN 2017, Valencia, Spain, 3–5 July 2017.
20. Ponce-Farfán, C.; Santillán, D.; Toledo, M.Á. Thermal Simulation of Rolled Concrete Dams: Influence of the Hydration Model and the Environmental Actions on the Thermal Field. *Water* **2020**, *12*, 858. [CrossRef]
21. Oliveira, R.G.; Rodrigues, J.P.C.; Pereira, J.M.; Lourenço, P.B.; Lopes, R.F.R. Experimental and Numerical Analysis on the Structural Fire Behaviour of Three–Cell Hollowed Concrete Masonry Walls. *Eng. Struct.* **2021**, *228*, 111439. [CrossRef]
22. Prakash, P.R.; Azenha, M.; Pereira, J.M.; Lourenço, P.B. Finite Element Based Micro Modelling of Masonry Walls Subjected to Fire Exposure: Framework Validation and Structural Implications. *Eng. Struct.* **2020**, *213*, 110545. [CrossRef]
23. Khoshbakht, M.; Lin, M.W. A Finite Element Model for Hygro-Thermo-Mechanical Analysis of Masonry Walls with FRP Reinforcement. *Finite Elem. Anal. Des.* **2010**, *46*, 783–791. [CrossRef]
24. Ramézani, H.; Jeong, J. Environmentally Motivated Modeling of Hygro-Thermally Induced Stresses in the Layered Limestone Masonry Structures: Physical Motivation and Numerical Modeling. *Acta Mech.* **2011**, *220*, 107–137. [CrossRef]
25. Castellazzi, G.; Colla, C.; de Miranda, S.; Formica, G.; Gabrielli, E.; Molari, L.; Ubertini, F. A Coupled Multiphase Model for Hygrothermal Analysis of Masonry Structures and Prediction of Stress Induced by Salt Crystallization. *Constr. Build. Mater.* **2013**, *41*, 717–731. [CrossRef]
26. Koniorczyk, M.; Gawin, D. Modelling of Salt Crystallization in Building Materials with Microstructure–Poromechanical Approach. *Constr. Build. Mater.* **2012**, *36*, 860–873. [CrossRef]

27. Derluyn, H.; Moonen, P.; Carmeliet, J. Deformation and Damage Due to Drying-Induced Salt Crystallization in Porous Limestone. *J. Mech. Phys. Solids* **2014**, *63*, 242–255. [CrossRef]
28. Choo, J.; Sun, W. Cracking and Damage from Crystallization in Pores: Coupled Chemo-Hydro-Mechanics and Phase-Field Modeling. *Comput. Methods Appl. Mech. Eng.* **2018**, *335*, 347–379. [CrossRef]
29. Castellazzi, G.; de Miranda, S.; Grementieri, L.; Molari, L.; Ubertini, F. Multiphase Model for Hygrothermal Analysis of Porous Media with Salt Crystallization and Hydration. *Mater. Struct.* **2016**, *49*, 1039–1063. [CrossRef]
30. Grementieri, L.; Daghia, F.; Molari, L.; Castellazzi, G.; Derluyn, H.; Cnudde, V.; de Miranda, S. A Multi-Scale Approach for the Analysis of the Mechanical Effects of Salt Crystallisation in Porous Media. *Int. J. Solids Struct.* **2017**, *126–127*, 225–239. [CrossRef]
31. de Miranda, S.; D'Altri, A.M.; Castellazzi, G. Modeling Environmental Ageing in Masonry Strengthened with Composites. *Eng. Struct.* **2019**, *201*, 109773. [CrossRef]
32. Mertens, S. Hysteresis, Damage and Moisture Effects in Quasi-Brittle Porous Materials. Ph.D. Thesis, Katholieke Universiteit Leuven, Leuven, Belgium, 2009.
33. Carmeliet, J. Influence of Damage and Moisture on the Nonlinear Hysteretic Behavior of Quasi-Brittle Materials. In *Nonlinear Elasticity and Hysteresis: Fluid-Solid Coupling in Porous Media*; Kim, A.H., Guyer, R.A., Eds.; Wiley-VCH Verlag GmbH & Co. KGaA: Weinheim, Germany, 2015; pp. 81–104. ISBN 9783527665068.
34. Lourenço, P.B. Computational Strategies for Masonry Structures. Ph.D. Thesis, Delft University, Delft, The Netherlands, 1996.
35. D'Altri, A.M.; de Miranda, S.; Castellazzi, G.; Sarhosis, V. A 3D Detailed Micro–Model for the in–Plane and out–of–Plane Numerical Analysis of Masonry Panels. *Comput. Struct.* **2018**, *206*, 18–30. [CrossRef]
36. Petracca, M.; Pelà, L.; Rossi, R.; Zaghi, S.; Camata, G.; Spacone, E. Micro–Scale Continuous and Discrete Numerical Models for Nonlinear Analysis of Masonry Shear Walls. *Constr. Build. Mater.* **2017**, *149*, 296–314. [CrossRef]
37. Ramirez, R.; Ghiassi, B.; Pineda, P.; Lourenço, P.B. Simulation of Moisture Transport in Fired-Clay Brick Masonry Structures Accounting for Interfacial Phenomena. *Build. Environ.* **2023**, *228*, 109838. [CrossRef]
38. Künzel, H.M. Simultaneous Heat and Moisture Transport in Building Components: One– and Two–Dimensional Calculation Using Simple Parameters. Ph.D. Thesis, Fraunhofer Institute for Building Physics, Stuttgart, Germany, 1995.
39. Bergman, T.L.; Lavine, A.S. *Fundamentals of Heat and Mass Transfer*, 8th ed.; John Wiley & Sons: Hoboken, NJ, USA, 2017; ISBN 978-1-119-32042-5.
40. Cammerer, W.F. *Wärme- Und Kälteschutz Im Bauwesen Und in Der Industrie*, 5th ed.; Springer: Berlin/Heidelberg, Germany, 1995; ISBN 978-3-642-78636-5.
41. HAMSTAD Reports: Hagentoft, C.E.; Adan, O.; Adl-Zarrabi, B.; Becker, R.; Brocken, H.; Carmeliet, J.; Djebbar, R.; Funk, M.; Grunewald, J.; Hens, H.; et al. *HAMSTAD Work Package 2: Final Report—Benchmark Package*; Chalmers University of Technology: Gothenburg, Sweden, 2003.
42. Janssen, H.; Blocken, B.; Carmeliet, J. Conservative Modelling of the Moisture and Heat Transfer in Building Components under Atmospheric Excitation. *Int. J. Heat. Mass. Transf.* **2007**, *50*, 1128–1140. [CrossRef]
43. Defraeye, T.; Blocken, B.; Carmeliet, J. Influence of Uncertainty in Heat–Moisture Transport Properties on Convective Drying of Porous Materials by Numerical Modelling. *Chem. Eng. Res. Des.* **2013**, *91*, 36–42. [CrossRef]
44. Feng, C.; Janssen, H. Hygric Properties of Porous Building Materials (II): Analysis of Temperature Influence. *Build. Environ.* **2016**, *99*, 107–118. [CrossRef]
45. Salager, S.; Youssoufi, M.S.E.; Saix, C. Influence of Temperature on the Water Retention Curve of Soils. Modelling and Experiments. In *Experimental Unsaturated Soil Mechanics*; Schanz, T., Ed.; Springer: Berlin/Heidelberg, Germany, 2007; pp. 251–258.
46. Kell, G.S. Density, Thermal Expansivity, and Compressibility of Liquid Water from 0° to 150°: Correlations and Tables for Atmospheric Pressure and Saturation Reviewed and Expressed on 1968 Temperature Scale. *J. Chem. Eng. Data* **1975**, *20*, 97–105. [CrossRef]
47. Hansen, K.K. *Sorption Isotherms. A Catalogue*; Technical University of Denmark (DTU): Lyngby, Denmark, 1986.
48. Pavlík, Z.; Žumár, J.; Medved, I.; Černý, R. Water Vapor Adsorption in Porous Building Materials: Experimental Measurement and Theoretical Analysis. *Transp. Porous Media* **2012**, *91*, 939–954. [CrossRef]
49. Castellazzi, G.; de Miranda, S.; Grementieri, L.; Molari, L.; Ubertini, F. Modelling of Non-Isothermal Salt Transport and Crystallization in Historic Masonry. *Key Eng. Mater.* **2014**, *624*, 222–229. [CrossRef]
50. Schirmer, R. Die Diffusionswiderstandszahl von Wasserdampf-Luftgemischen Und Die Verdampfungsgeschwindigkeit. *VDI Beih. Verfahr.* **1938**, *6*, 170–177.
51. Murray, F.W. On the Computation of Saturation Vapor Pressure. *J. Appl. Meteorol.* **1967**, *6*, 203–204. [CrossRef]
52. Monteith, J.L.; Shatleworth, M.H. *Principles of Environmental Physics*, 4th ed.; Elsevier Ltd.: London, UK, 2013; ISBN 9780123869937.
53. Gummerson, R.J.; Hall, C.; Hoff, W.D. Water Movement in Porous Building Materials II. Hydraulic Suction and Sorptivity of Brick and Other Masonry Materials. *Build. Environ.* **1980**, *15*, 101–108. [CrossRef]
54. Guizzardi, M.; Derome, D.; Carmeliet, J. Water Uptake in Clay Brick at Different Temperatures: Experiments and Numerical Simulations. *J. Build. Phys.* **2016**, *39*, 373–389. [CrossRef]
55. Feng, C.; Janssen, H. The Influence of Temperature on the Capillary Absorption Coefficient-A Confrontation of Two Recent Papers in Building and Environment. *Build. Environ.* **2017**, *116*, 257–258. [CrossRef]
56. Hanumanthu, K.; Sarkar, K. Statistical Quantification of the Effect of Temperature on Capillary Water Absorption in Some Porous Building Materials. *Build. Environ.* **2021**, *198*, 107889. [CrossRef]

57. Washburn, E.W. The Dynamics of Capillary Flow. *Phys. Rev.* **1921**, *17*, 273–283. [CrossRef]
58. Karagiannis, N.; Karoglou, M.; Bakolas, A.; Moropoulou, A. Building Materials Capillary Rise Coefficient: Concepts, Determination and Parameters Involved. In *New Approaches to Building Pathology and Durability. Building Pathology and Rehabilitation*; Delgado, J.M.P.Q., Ed.; Springer: Singapore, 2016; Volume 6, pp. 27–44.
59. *COMSOL COMSOL Multiphysics®*, 6th ed.; COMSOL AB: Stockholm, Sweden, 2021.
60. Climate and Average Weather Year–Round in Guimarães, Portugal. Available online: https://weatherspark.com/y/32437/Average-Weather-in-Guimar%C3%A3es-Portugal-Year-Round (accessed on 1 October 2022).
61. Hagentoft, C.E.; Kalagasidis, A.S.; Adl-Zarrabi, B.; Roels, S.; Carmeliet, J.; Hens, H.; Grunewald, J.; Funk, M.; Becker, R.; Shamir, D.; et al. Assessment Method of Numerical Prediction Models for Combined Heat, Air and Moisture Transfer in Building Components: Benchmarks for One-Dimensional Cases. *J. Therm. Envel. Build. Sci.* **2004**, *27*, 327–352. [CrossRef]
62. Kočí, V.; Čáchová, M.; Koňáková, D.; Vejmelková, E.; Jerman, M.; Keppert, M.; Maděra, J.; Černý, R. Heat and Moisture Transport and Storage Parameters of Bricks Affected by the Environment. *Int. J. Thermophys.* **2018**, *39*, 63. [CrossRef]
63. Prangnell, R.D. The Water Vapour Resistivity of Building Materials: A Literature Survey. *Matériaux Constr.* **1971**, *4*, 399–405. [CrossRef]
64. Kumaran, K. *IEA Annex 24: Heat, Air and Moisture Transfer in Insulated Envelope Parts. Final Report, Volume 3, Taks 3: Material Properties*; Katholieke Universiteit Leuven: Leuven, Belgium, 1996.
65. Szekeres, A. Thermo-Hygro-Elasticity (THE). In *Encyclopedia of Thermal Stresses*; Hetnarski, R.B., Ed.; Springer: Berlin/Heidelberg, Germany, 2014; pp. 5918–5924. ISBN 978-94-007-2738-0.
66. Carmeliet, J.; Derome, D.; Dressler, M.; Guyer, R.A. Nonlinear Poro-Elastic Model for Unsaturated Porous Solids. *J. Appl. Mech.* **2013**, *80*, 020909. [CrossRef]
67. Ghiassi, B.; Oliveira, D.V.; Lourenço, P.B.; Marcari, G. Numerical Study of the Role of Mortar Joints in the Bond Behavior of FRP-Strengthened Masonry. *Compos. B Eng.* **2013**, *46*, 21–30. [CrossRef]
68. Penas, F.; Veiga, R.; Gomes, A. Hydraulic Lime Mortars to Use in Old Buildings: Advantages and Drawbacks. In Proceedings of the HMC08—1st Historical Mortars Conference 2008: Characterization, Diagnosis, Conservation, Repair and Compatibility, Lisbon, Portugal, 24–26 September 2008; Laboratório Nacional de Engenharia Civil (LNEC): Lisbon, Portugal, 2008.